Geophysical Journal International

Geophys. J. Int. (2013) doi: 10.1093/gji/ggt004

Geophysical Journal International Advance Access published February 5, 2013

Distinguishing eclogite from peridotite: EBSD-based calculations of seismic velocities

James R. Worthington,[1,*] Bradley R. Hacker[1] and George Zandt[2]

[1]*Department of Earth Science, University of California, Santa Barbara, California, USA. E-mail: jamesworthington@email.arizona.edu*
[2]*Department of Geosciences, University of Arizona, Tucson, Arizona, USA*

Accepted 2013 January 4. Received 2012 October 31; in original form 2012 August 3

SUMMARY

Seismic velocities were calculated for 11 eclogites from the Western Gneiss Region, Norway, based on electron-backscatter diffraction (EBSD). The *P*-wave velocities are 8.0–8.5 km s^{-1} and the *S*-wave velocities are 4.5–4.8 km s^{-1}; V_P/V_{S1} (the ratio of *P*-wave to fast *S*-wave velocities) is 1.74–1.81. All the eclogites are relatively isotropic, with the higher anisotropies (3–4 per cent) in micaceous samples. Peridotite is comparatively more anisotropic (4–14 per cent more for *P* waves and up to 10 per cent more for *S* waves), and can have anomalously low V_P/V_{S1}, which may be useful means of distinguishing it from eclogite. Micaceous eclogite may be modelled using hexagonal anisotropy with a slow unique axis, whereas peridotite is most robustly modelled using orthorhombic anisotropy.

Key words: Composition of the mantle; Body waves; Surface waves and free oscillations; Seismic anisotropy; Acoustic properties; Dynamics of lithosphere and mantle.

1 INTRODUCTION

While seismic anisotropy in the mantle has been chiefly interpreted as reflecting the crystallographic preferred orientation (CPO) of olivine caused by mantle flow (e.g. Hess 1964), utilizing anisotropy to identify the volume and distribution of mafic rocks in Earth's upper mantle and lower crust is central to advancing our understanding of geodynamics (e.g. Hetényi *et al.* 2007; Monsalve *et al.* 2008). Physical property measurements (Christensen 1979; Christensen 1996) and calculations derived from mineral physical properties (e.g. Hacker *et al.* 2003) indicate that typical peridotite and eclogite have essentially the same isotropic velocities and are therefore indistinguishable at depth within Earth. Several features render this conclusion worthy of further investigation, however: (i) eclogites have a range of compositions other than MORB (Coleman *et al.* 1965); (ii) not all peridotite is the same composition; (iii) eclogite and peridotite can have anisotropic velocities. This contribution assesses whether it is possible to distinguish eclogite from peridotite using seismic velocities or velocity anisotropies, by comparing the elastic properties of a range of eclogite and peridotite compositions.

Although 'bimineralic' eclogite typically consists of garnet and omphacite with minor rutile, other minerals are stable in bulk compositions different from basalt. Phengite ± kyanite are stabilized by elevated K_2O or Al_2O_3 and orthopyroxene ± biotite are stabile in picritic or pyroxenitic eclogite with elevated MgO and depleted CaO (Nakamura 2003). Lawsonite, amphibole and/or zoisite are stable in some low-temperature eclogite (Poli & Schmidt 1998). This paper quantifies the seismic signature of eleven eclogite samples. We conclude that even strongly deformed eclogite is indeed essentially isotropic, with the exception of micaceous end-member compositions, whose compressional wave anisotropy is 3–4 per cent. Eclogite velocities are within the range of those calculated for peridotite, which can be considerably more anisotropic.

The eclogite samples come from the Western Gneiss Region (WGR, Fig. 1), a polymetamorphic terrane in southwestern Norway, formed during the Caledonian collision of Baltica and Laurentia (Eskola 1921; Krogh 1977). In particular, these eclogites formed in deeply subducted portions of the Baltica quartzofeldspathic craton where temperatures reached 850°C and pressures reached 3.6 GPa during the Scandian UHP–HP phase (425–400 Ma) of the Caledonian orogeny (Cuthbert *et al.* 2000; Hacker 2006). The samples are minimally or non-retrogressed, and any alteration was purposefully ignored when calculating physical properties. We compare these eclogites to a range of peridotite samples reported in the literature.

2 SEISMIC ANISOTROPY

Minerals are elastically anisotropic, and when aligned, impart a directional dependence to *P*- and *S*-wave velocity and polarization direction (e.g. Mainprice 2007). Shear waves split into orthogonally polarized fast (S_1) and slow (S_2) components when propagating through an anisotropic medium (Silver 1996), and the magnitude and orientation of this splitting are functions of the medium's elastic symmetry (as described by the Christoffel tensor) and the wave propagation direction through the medium. Therefore, the delay time between fast and slow shear waves (δt) and the azimuthal

* Now at: University of Arizona, Tucson, USA.

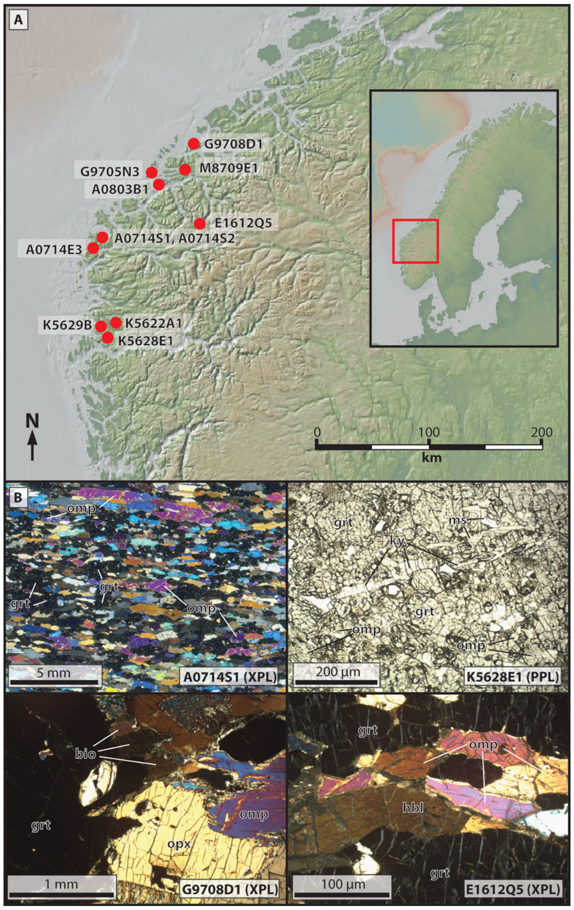

Figure 1. (a) Locations of eclogite samples from the Western Gneiss Region, Norway. (b) Photomicrographs of eclogite samples with relevant phases indicated, using the abbreviations of Kretz (1983). Samples were selected to represent the range of common eclogite types, clockwise from top left: bimineralic eclogite, phengite ± kyanite eclogite, amphibole eclogite and orthopyroxene ± biotite eclogite (see text).

orientation of the fast shear wave's polarization plane (ϕ), which are recorded by seismometers at the surface, are common variables of interest in anisotropy studies. Whereas variations in δt and ϕ can indicate the presence and orientation of features in the shallow crust such as joints, veins and layering, the focus here is on the relationship of these variables to CPOs in eclogite and peridotite in the lower crust and upper mantle.

Shear-wave splitting is most commonly and successfully measured using SKS (and SKKS) waves, which are converted *P*-to-*S* phases that have passed through Earth's core. The utility of SKS waves lies in their known S_V polarization (independent of the earthquake's focal mechanism), which requires that any observed anisotropy is derived from the receiver side of the ray path out of the core (Savage 1999). The broad similarity between *S* waveforms from earthquakes deeper than 400 km and SKS waveforms indicates that the lower mantle is largely isotropic (e.g. Kaneshima & Silver 1995), with the exception of the D$''$ region of the lowermost mantle, which is commonly anisotropic (Wenk *et al.* 2011). Most studies have modelled the D$''$ region as hexagonally anisotropic with a vertical unique axis (Savage 1999), however, which yields negligible splitting for subvertically incident SKS waves. The lower mantle is thus effectively isotropic for SKS waves, such that any observed SKS splitting should result from anisotropy within the lithosphere and upper mantle.

SKS studies have the important restriction that only subvertically incident rays within the shear-wave window (incidence angle <35° from vertical) are used. This restriction derives from the fact that rays with greater incidence angles generate non-linear particle motion from post-critical *S*-to-*P* reflections at the surface, which distort the amplitude and phase of the recorded wave (Savage 1999). Therefore, the shear-wave window is included and discussed in this study where it is relevant, and a horizontal foliation is often assumed. The common technique of analysing shear-wave splitting in stacks of SKS signals in regional arrays of broad-band seismometers produces excellent lateral resolution but poor vertical resolution (Biryol *et al.* 2010) of lithospheric and upper-mantle structure below the array. Receiver functions, classically used to determine depths to interfaces, also provide useful information regarding the azimuthal variation in anisotropy, and are an effective tool for modelling layers of hexagonal isotropy in the lower crust (e.g. Porter *et al.* 2011) and upper mantle (e.g. Bostock 1999).

One means of obtaining improved vertical resolution of the lower crust and upper mantle involves inverting surface-wave dispersion data for *S*-wave structure (e.g. Bensen *et al.* 2008; Marone *et al.* 2008; Warren *et al.* 2008). Because surface waves are frequency-dispersive, they sample a continuum of depths as a function of frequency. Coupling this depth sensitivity with discrepancies between Rayleigh and Love waves provides a means of identifying zones of radial anisotropy in the crust (e.g. Shapiro *et al.* 2004) and mantle (e.g. Ekström & Dziewonski 1998). Inverting long-period surface waves for *S*-wave structure in the upper mantle provides improved vertical resolution but poorer lateral resolution, although this can be improved by implementing arrays of seismometers. In addition to improved depth resolution, surface waves are not restricted to the shear-wave window, and may, therefore, sample more complete 3-D variation in anisotropy of eclogite and peridotite. This may improve the characterization of azimuthal anisotropy in regions that are outside the effective shear-wave window of extant seismic arrays, for instance.

The most coherent means of assessing the structure of the lower crust and upper mantle is to utilize the strengths of the various seismic methods relevant to these depths. The role of this and similar studies is to provide the seismology community with predictive information regarding the 3-D velocity and anisotropy characteristics of rocks expected in these tectonic settings, which include subduction zones, orogenic roots and Rayleigh–Taylor instabilities.

2.1 Display scheme for seismic velocities

Various methods have been used to display seismic anisotropy in minerals and rocks. One method, common in studies that measure rock velocities, is to list velocities in three mutually perpendicular directions (with respect to lineation and foliation) in a table (e.g. Kern *et al.* 1999). This provides a first-order means of assessing anisotropy but is incomplete. Another method is to plot velocities along directional traverses between crystallographic directions in minerals or structural directions in rocks (e.g. Weiss *et al.* 1999). This paper uses stereographic projections (stereonets) to display complete 3-D variation of seismic parameters in minerals and rocks. Because an elastic tensor (which defines the distribution of *P* and *S* velocities and polarizations) is a centrosymmetric property of an elastic medium (Mainprice 2007), forward and reverse senses of ray propagation in any direction have equivalent seismic properties. Thus, a single hemisphere is sufficient to describe the full range of seismic anisotropy in rocks and minerals.

Table 1. Mineralogies of eclogite and peridotite samples. Densities in g cm^{-3}. Mineral abbreviations are from Kretz (1983): Bt = biotite; Grt = garnet; Hbl = hornblende; Ky = kyanite; Ol = olivine; Omp = omphacite; Opx = orthopyroxene; Ms = muscovite (phengite); Qtz = quartz; Rut = rutile; Zo = zoisite.

Sample	Type	Density (g cm^{-3})	Mineralogy
A0714E3	Amphibole eclogite	3.58	0.51 Omp, 0.34 Grt, 0.11 Hbl, 0.02 Ms, 0.01 Qtz, 0.01 Rt
A0714S1	Omp + Grt eclogite	3.58	0.60 Omp, 0.35 Grt, 0.05 Qtz
A0714S2	Ky + Phg eclogite	3.58	0.62 Omp, 0.32 Grt, 0.04 Ky, 0.02 Ms
A0803B1	Opx eclogite	3.58	0.51 Omp, 0.26 Grt, 0.16 Opx, 0.04 Rt, 0.03 Hbl
E1612Q5	Phg amphibole eclogite	3.58	0.53 Omp, 0.35 Grt, 0.08 Hbl, 0.03 Ms, 0.01 Qtz + Rt
G9705N3	Ky + Bt eclogite	3.72	0.47 Omp, 0.45 Grt, 0.03 Bt, 0.02 Ky, 0.02 Qtz, 0.01 Rt
G9708D1	Opx + Bt eclogite	3.70	0.48 Gar, 0.33 Omp, 0.09 Bt, 0.06 Opx, 0.03 Hbl (retrograde), 0.01 Rt
K5622A1	Phg ampibole eclogite	3.74	0.52 Gar, 0.31 Omp, 0.08 Hbl, 0.05 Ms, 0.02 Rt, 0.01 Qtz, 0.01 Ky
K5628E1	Phg + Ky Zo-amphibole eclogite	3.71	0.50 Gar, 0.35 Omp, 0.05 Hbl, 0.03 Ms, 0.03 Ky, 0.03 Zo, 0.01 Qtz
K5629B	Phg + Ky Zo-amphibole eclogite	3.57	0.38 Gar, 0.36 Omp, 0.13 Ms, 0.05 Hbl, 0.04 Ky, 0.02 Zo, 0.01 Qtz, 0.01 Rt
M8709E1	Omp + Grt eclogite	3.71	0.50 Omp, 0.41 Gar, 0.07 Hbl (retrograde), 0.02 Rt
Italy	Peridotite	3.31	0.70 Ol, 0.30 Opx
Bernard	Peridotite	3.36	0.85 Ol, 0.15 Opx
Finero	Peridotite	3.36	0.85 Ol, 0.10 Bt, 0.05 Opx

We use the following naming conventions: V_P = P-wave velocity, V_S = isotropic shear-wave velocity, V_{S1} = fast shear-wave velocity, V_{S2} = slow shear-wave velocity, AV_{S1} = fast shear-wave anisotropy (per cent), AV_{S2} = slow shear-wave anisotropy (per cent), δV_S = shear-wave splitting, V_P/V_{S1} = P-wave to fast shear-wave ratio, V_P/V_{S2} = P-wave to slow shear-wave ratio. Additionally, we use standard crystallographic notation where (UVW) represents a crystallographic direction, (hkl) represents a crystallographic plane (Miller index), and (UVW)∗ represents the pole to a crystallographic plane. Crystallographic [100], [010], and [001] directions correspond to *a*, *b*, and *c* directions, respectively, in the common alternative notation. We use *X*, *Y* and *Z* to represent mutually orthogonal principal directions with respect to the rock fabric: *X* is the lineation, *Z* is the pole to the foliation, and *Y* is perpendicular to both.

3 METHODS

3.1 Sample selection and mineralogy

Eleven eclogite thin sections from the WGR were analysed in this study (Table 1; Appendix). The samples were selected to represent the range of common eclogite types: (1) bimineralic, omphacite + garnet eclogite, (2) phengite ± kyanite eclogite, (3) orthopyroxene ± biotite eclogite and (4) amphibole eclogite; all eclogites contain other trace phase such as rutile, quartz, coesite, zircon and/or apatite. The modal abundances of minerals for each sample were determined by point counting with an optical microscope and calculated from elemental abundances obtained with an energy-dispersive spectrometer (EDS) on an FEI Q400 FEG scanning electron microscope (SEM). The EDS data were collected using a 20 kV accelerating voltage and a working distance of 10 mm. A MATLAB routine written by Sarah Brownlee was used to determine the proportions of each phase.

3.2 Determination of CPOs

The CPOs were measured using an HKL electron-backscatter diffraction (EBSD) detector on the SEM. The thin sections were polished using colloidal silica to remove mechanical polishing damage, and were examined uncoated in the SEM in low-vacuum mode with an accelerating voltage of 20 kV and a working distance of ∼10 mm. The thin sections were tilted at 70° from horizontal. HKL's CHANNEL5 software was used to index and map crystals with a step size of up to 100 μm. The CPO maps were processed into 1-point-per-grain (PPG) data sets by extrapolating wild spikes using all nearest neighbours, a grain-boundary misorientation of 10° and considering only grains larger than 0.04 mm^2. The samples are not geographically oriented, and the unfoliated samples were cut arbitrarily. A common orientation was established by rotating the CPOs for obliquely cut samples such that the clinopyroxene [001] CPO is parallel to the lineation (samples A0714S1, A0714S2, G9705N3 and G9708D1 were not rotated).

3.3 Determination of seismic velocities at STP and 'peak conditions'

The CPO data were processed using the software of Mainprice 1990. Mainprice's *PFch5.exe* program was used to plot lower hemisphere, equal-area pole figures in the *XZ* reference frame. Crystal symmetry considerations (e.g. Nye 1957) enable the reduction of the fourth-rank elasticity tensor into a 6 × 6 stiffness matrix, which is the conventional means of describing material elastic properties. Using single-crystal 6 × 6 stiffness matrices and the calculated modal abundances, whole-rock stiffness matrices and seismic properties of the eclogites were calculated with *ANISch5.exe* and averaged via the Voigt–Reuss–Hill method. Retrograde amphibole, biotite and chlorite were specifically ignored so that the calculations reflect eclogite-facies conditions. *EMATRIX6.exe* was used to rotate the elastic constants into the *XY* reference frame, to introduce phengite CPOs into the relevant eclogites, to compute a 'grand average' of all 11 eclogites samples, and to synthesize biotite, orthopyroxene and olivine CPOs for the 'Finero' peridotite (see below).

The single-crystal stiffness matrices that we used in our seismic velocity calculations are summarized in Table 2. For the kyanite-bearing eclogites, we have used Vaughan & Weidner's (1978) sillimanite stiffness matrix in lieu of Winkler *et al.*'s (2001) kyanite stiffness matrix because the former is experimentally derived and represents STP conditions, whereas the latter is derived through quantum mechanical calculations and represents a temperature of 0 K. All the stiffness matrices in Table 2 are experimentally derived and represent STP conditions, and we have performed this

Table 2. References for single-crystal stiffness matrices used for seismic velocity calculations in this study. Sillimanite has been used in lieu of kyanite (see text).

Mineral	Reference
Biotite	Aleksandrov & Ryzhova (1961b)
Coesite	Angel *et al.* (2001)
Garnet	Babuska *et al.* (1978)
Hornblende	Aleksandrov & Ryzhova (1961a)
Sillimanite	Vaughan & Weidner (1978)
Olivine	Bhagat & Bass (1992)
Omphacite	Abramson *et al.* (1997)
Orthopyroxene	Webb & Jackson (1993)
Phengite	Vaughan & Guggenheim (1986)
Quartz	Lakshtanov *et al.* (2007)
Rutile	Bass (1995)
Zoisite	Mao *et al.* (2007)

'substitution' to maintain a uniform methodology in our seismic velocity calculations. In addition, we use the coesite stiffness matrix of Angel *et al.* (2001) instead of that by Weidner & Carleton (1977) because the former corrected an erroneous value in the latter's stiffness matrix. Finally, as a technical note, we use Vaughan & Guggenheim's (1986) stiffness tensor for muscovite as an approximation of phengite, which is very similar in composition and crystal structure to muscovite but a more characteristic component of eclogite mineral assemblages.

The Mainprice-based calculations represent STP conditions because the single-crystal stiffness matrices were measured at STP. The pressure and temperature dependencies of the stiffness matrices of few minerals have been measured or calculated. To circumvent this limitation and calculate velocities at high pressure and high temperature, we used the macro of Hacker & Abers (2004) to calculate isotropic rock velocities at STP and 'peak conditions' of 3.0 GPa/750°C and then simply scaled the anisotropic velocities by the same ratio. Because our 'peak conditions' are in the coesite stability field, we used a coesite stiffness matrix to calculate and scale the 'peak' anisotropic velocities of rocks containing quartz. Mainprice's *VpG.exe* program was then used to produce lower-hemisphere, equal-area seismic-velocity stereonets of the scaled eclogites and peridotites in an *XY* reference frame. MATLAB code written by Bradley Hacker and Sarah Brownlee was used to plot V_P/V_{S1} versus V_{S1} within the shear-wave window (a 35° cone around the *Z* direction).

We compare our calculated eclogite velocities to three peridotite samples that are representative of a broad range of peridotite compositions and mineralogies (Hacker & Abers 2012). The first, 'Italy', is an average of 15 peridotite (mainly dunite and harzburgite) xenoliths from central Italy (Pera *et al.* 2003) that have the 'type-A' olivine CPO of Karato *et al.* (2008). The second, 'Bernard', is an average of 17 harzburgite samples from Bernard Mountain in the Talkeetna arc of Alaska (Mehl *et al.* 2003; Hacker 2008) that have the 'type-E' olivine CPO of Karato *et al.* (2008). The third, 'Finero', was created using mineral abundances from Cawthorn's (1975) phlogopite peridotite from the Finero complex of the Ivrea–Verbano zone in northern Italy, a 'type-A' olivine CPO (Karato *et al.* 2008), a typical orthopyroxene CPO with [100] axes perpendicular to the lineation (Soustelle *et al.* 2010) and a phlogopite CPO with (001) parallel to the foliation. The 'Italy' and 'Bernard' peridotites represent partially depleted upper mantle and 'Finero' represents hydrated upper mantle.

4 RESULTS

4.1 Measured CPOs

The measured CPOs of the principal phases in the eclogites are compiled in Fig. 2. The garnet CPOs are weak in all samples. The dominant omphacite CPO is a strong [001] maximum subparallel to the lineation and a (010) maximum perpendicular to the foliation; three samples, A0803B1, K5622A1 and K5629B have weaker [001] maxima parallel to the lineation and (010) distributed in a girdle perpendicular to the lineation. Each amphibole CPO tends to be similar to the omphacite CPO from the same sample. Orthopyroxene has [001] maxima parallel to lineation and either [100] or [010] subparallel to the foliation. The zoisite CPOs are characterized by [100] maxima perpendicular to the foliation and [010] maxima parallel to the lineation. A CPO for rutile was measured in one sample, and shows a [001] maximum canted 45° to the foliation; the other two principal directions define girdles. A kyanite CPO measured in one sample has a [001] maximum parallel to the lineation and [100] parallel to the foliation.

In two of the mica-bearing eclogites (A0714S2, K5622A1), the (001) planes of the mica are parallel to the foliation, as expected. In six other micaceous samples (A0714E3, A0714S2, E1612Q5, G9705N3, G9708D1, K5628E1), the indexed mica grains have (001) maxima perpendicular the foliation. This CPO is impossible because the mica sheets are subparallel to the foliation in thin section; it is a product of EBSD indexing bias because the mica is so much softer than the other eclogite minerals that it polishes poorly. When calculating velocities, the mica CPOs from these samples were replaced by the phengite CPO from K5622A1.

4.2 Comparison of CPOs to previous studies

The CPOs obtained in this study are generally similar to those measured from other eclogites. The most-common omphacite CPO we observed—with [001] parallel to the lineation and (010) perpendicular to the foliation—was reported by Mauler *et al.* (2000), Bascou *et al.* (2001) and Abalos *et al.* (2011). The less common CPO, with a (010) girdle perpendicular to the lineation, was reported by Ji *et al.* (2003) and Abalos *et al.* (2011). The omphacite CPOs suggest a constrictional strain for all samples except A0803B1 and K5622A1, whose foliation-parallel [001] girdles suggest a flattening strain (e.g. Helmstaedt *et al.* 1972; Bascou *et al.* 2001).

The weak garnet CPOs are typical of eclogite (Mainprice *et al.* 2004). One of the zoisite CPOs is similar to one reported from a gneiss from the Papua New Guinea UHP terrane (Brownlee *et al.* 2011); the other is new. In aggregate, three of the four zoisite CPOs we know of (this study and that of Brownlee *et al.* 2011) suggest slip in the [010] direction along the (100) plane. The [001] maximum measured for rutile matches that seen in other studies (Bascou *et al.* 2001; Ji *et al.* 2003). The kyanite CPO has the same [001] direction parallel to the sillimanite measured by Erdman *et al.* (in review), but has (100), rather than (010), parallel to the foliation. The amphibole CPOs are expected from unit-cell considerations (Hacker & Christie 1990) and [001] maxima closely resemble previous studies of amphibole (Aspiroz *et al.* 2007; Tatham *et al.* 2008; Pearce *et al.* 2011). The orthorhombic symmetry of the CPOs and their coaxial orientation with respect to the foliation and lineation implies that the overall history was coaxial plane strain in most samples and perhaps coaxial constriction in K5622A1 and K5629B.

4.3 Single-crystal velocities

Because the 3-D seismic velocity structure of single crystals exerts the most fundamental influence on rock velocity, considering the variability of mineral seismic velocities is essential in relating rock mineralogy and CPOs to seismic signature. Fig. 3 shows crystallographically oriented stereonets of single-crystal seismic parameters for minerals common in eclogite and peridotite. The single-crystal properties are not discussed in detail here, but rather are provided as a reference to help the reader discern the origin of the whole-rock velocities. In general, Fig. 3 illustrates how crystal symmetry is manifested through seismic velocities. Cubic symmetry in garnet,

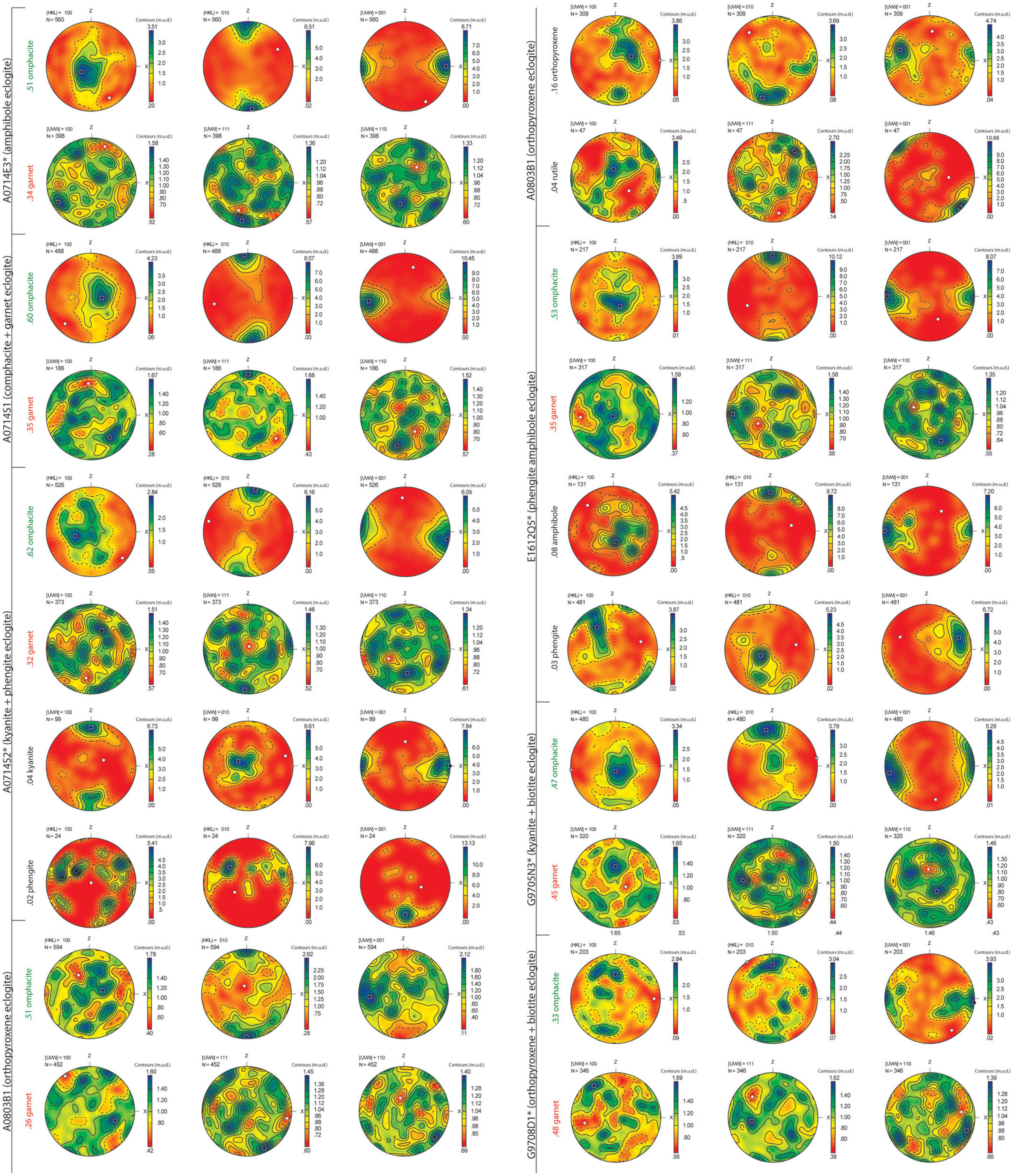

Figure 2.

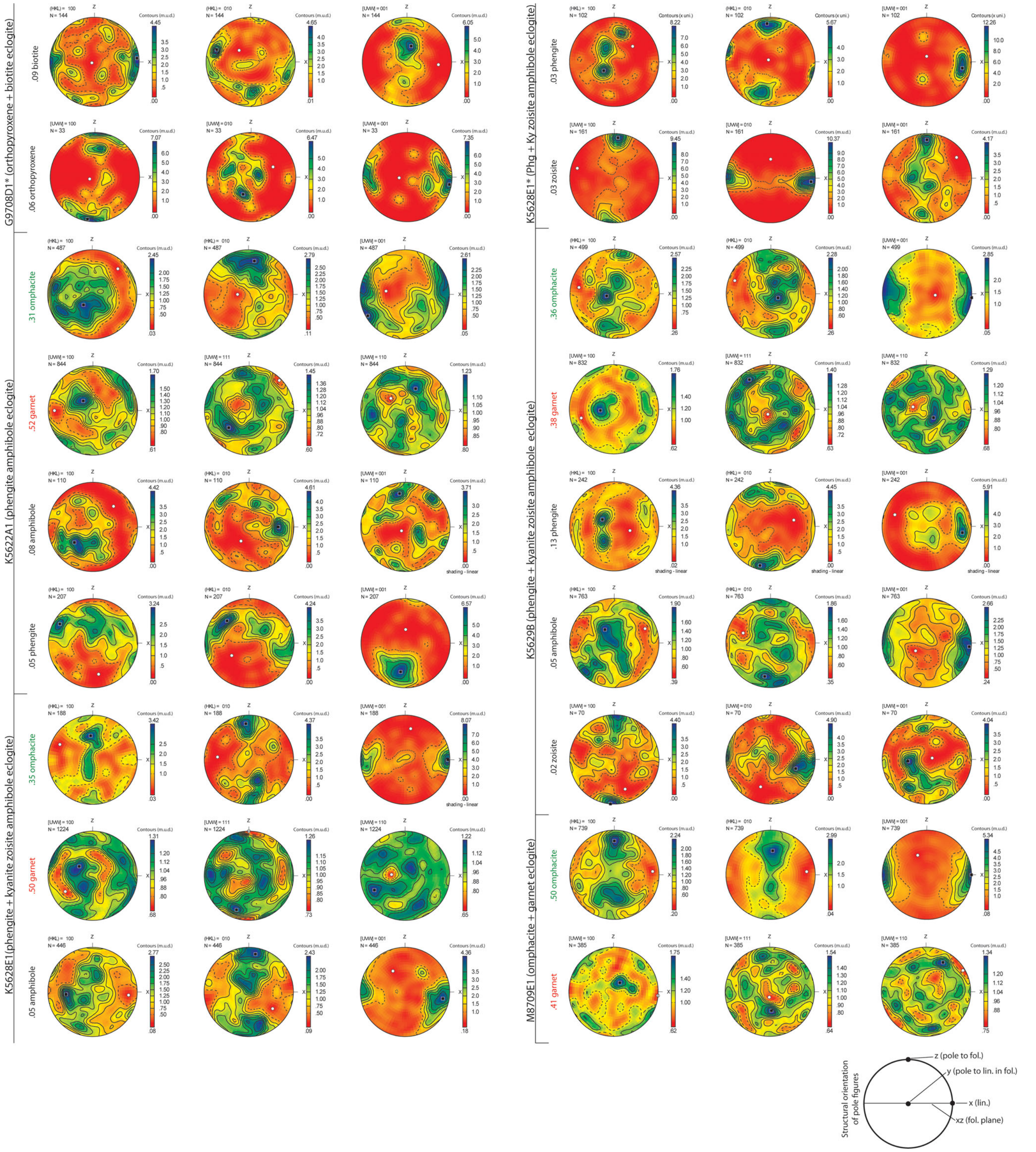

Figure 2. (This page and previous page) Lower-hemisphere pole figures (stereographically projected) of selected mineral phases for all eclogite samples, oriented in the XZ (structural) reference frame as shown. Contours are in multiples of uniform distribution (m.u.d.) and on a 1 point-per-grain (1 PPG) basis. Number preceding phase indicates modal abundance. [UVW] denotes crystallographic directions and (HKL) denotes poles to (hkl) crystallographic planes, which are equivalent to [UVW]*. *N* indicates the number of grains for each pole figure. Eclogites with an asterisk (∗) next to the sample name indicate that the phengite CPO from K5622A1 was used to calculate the contribution of mica to seismic velocities for the sample (see text).

monoclinic symmetry in omphacite and hornblende, orthorhombic symmetry in orthopyroxene and olivine, and pseudohexagonal symmetry in phengite and biotite define whole-rock velocities in addition to CPOs and modal abundances of the phases.

4.4 Velocity scaling

The effect of increasing pressure and temperature varies with seismic parameter and depends chiefly on composition (Table 3). The velocity changes from STP to peak conditions are small in all

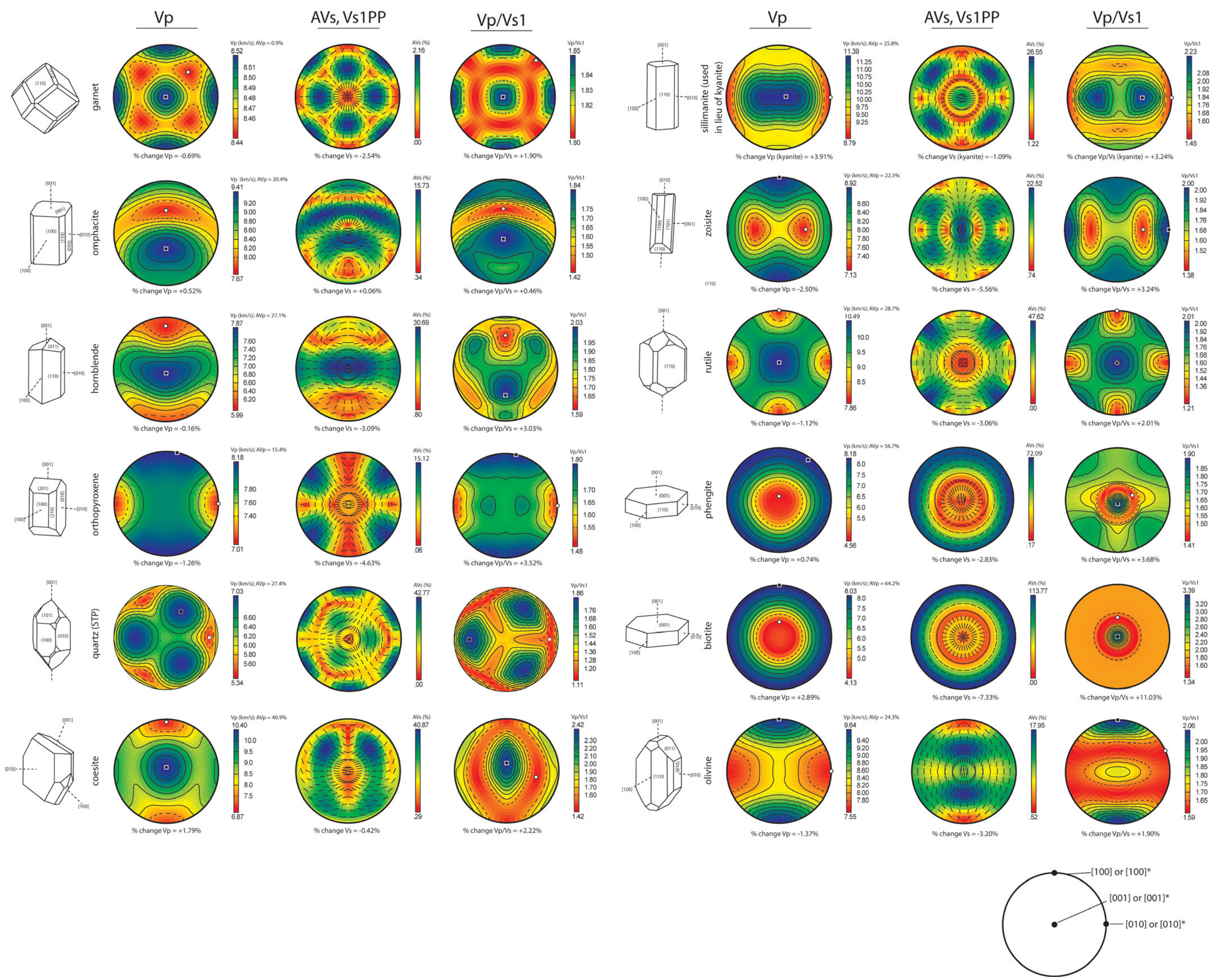

Figure 3. Lower-hemisphere, equal-area stereographic projections for single crystals of phases common in eclogite and peridotite, oriented in crystallographic reference frame as shown. Linear shading. Stereonets are grouped by mineral in columns as follows: left, *P*-wave velocity (V_P, km s^{-1}); centre, shear-wave anisotropy (AV_S, per cent) and fast shear-wave polarization plane (V_{S1}PP); right, V_P/V_{S1} ratio. Diagrams of crystal morphology (modified from Nesse 1991 with the exception of coesite, which is a conception) to the left of each set of stereonets show crystal symmetry and crystallographic directions for each mineral. Pressure-temperature conditions are 3.0 GPa and 750°C for all phases except quartz, which is calculated at STP. 'per cent change' under each velocity diagram indicates percent change in V_P, V_S and V_P/V_{S1} from STP to 'peak conditions'. Because the 3-D velocities are scaled by the same factor in all directions for V_P and V_S for each mineral, AV_P and AV_S do not change with temperature–pressure conditions.

Table 3. Seismic properties of eclogites and peridotites for all directions. V_P = *P*-wave velocity (km s^{-1}); AV$_P$ = *P*-wave anisotropy (per cent); V_{S1} = fast *S*-wave velocity (km s^{-1}); V_{S2} = slow *S*-wave velocity (km s^{-1}); AV_S = *S*-wave anisotropy (per cent); V_P/V_{S1} = *P*-wave:fast *S*-wave ratio; V_P/V_{S2} = *P*-wave:slow *S*-wave ratio. For each sample, top row gives calculations at STP, bottom row gives calculations at 'peak conditions' (3.0 GPa, 750°C). Values in parentheses indicate percent change of 'peak' value with respect to STP as calculated using the macro of Hacker & Abers (2004). AV_P, AV_{S1}, AV_{S2} and AV_S are unchanging with pressure and temperature for samples that do not contain quartz, so no change in these parameters between STP and 'peak conditions' is indicated. These parameters do change with pressure and temperature for samples with quartz due to the phase change from quartz to coesite at high pressures, however, so the change is indicated for relevant samples. For samples with quartz, STP calculations were performed using the stiffness matrix for quartz and 'peak' calculations were performed using the stiffness matrix for coesite, scaled from STP to 'peak conditions' using the macro of Hacker & Abers (2004).

Sample	V_P (km s^{-1})	AV_P (%)	V_{S1} (km s^{-1})	AV_{S1} (%)	V_{S2} (km s^{-1})	AV_{S2} (%)	AV_S (%)	V_P/V_{S1}	V_P/V_{S2}
A0714E3	8.10–8.26	2.0	4.63–4.69	1.2	4.60–4.65	1.0	0.06–1.70	1.73–1.78	1.75–1.79
	8.14–8.30 (+0.04%)	2.0 (+0.0%)	4.58–4.63 (−1.29%)	1.2 (+0.0%)	4.55–4.60 (−1.29%)	1.1 (+10.0%)	0.09–1.63 (−4.12%)	1.76–1.81 (+1.30%)	1.78–1.82 (+1.30%)
A0714S1	8.17–8.31	1.7	4.76–4.80	1.0	4.73–4.77	0.8	0.02–1.40	1.71–1.75	1.71–1.75
	8.35–8.50 (+2.24%)	1.7 (+0.0%)	4.74–4.80 (−0.21%)	1.1 (+10.0%)	4.74–4.76 (+0.00%)	0.6 (−25.0%)	0.02–1.14 (−18.6%)	1.75–1.79 (+2.31%)	1.75–1.79 (+2.31%)
A0714S2	8.34–8.51	2.0	4.81–4.86	0.9	4.80–4.84	0.8	0.02–1.06	1.73–1.76	1.73–1.77
	8.35–8.52 (+0.14%)		4.77–4.81 (−0.89%)		4.77–4.80 (−0.89%)			1.74–1.78 (+1.00%)	1.75–1.79 (+1.00%)
A0803B1	8.26–8.35	1.1	4.76–4.80	0.8	4.75–4.79	0.7	0.00–0.94	1.73–1.75	1.73–1.75
	8.25–8.34 (+0.17%)		4.69–4.72 (−1.61%)		4.68–4.71 (−1.61%)			1.75–1.77 (+1.45%)	1.75–1.78 (+1.45%)
E1612Q5	8.11–8.30	2.3	4.67–4.71	0.9	4.64–4.68	0.9	0.02–1.26	1.73–1.78	1.74–1.78
	8.16–8.35 (+0.61%)	2.3 (+0.0%)	4.62–4.66 (−1.06%)	0.8 (−11.1%)	4.59–4.63 (−1.07%)	0.9 (+0.0%)	0.04–1.26 (+0.00%)	1.76–1.80 (+1.43%)	1.77–1.81 (+1.70%)
G9705N3	8.33–8.48	1.7	4.76–4.82	1.1	4.73–4.78	1.1	0.00–1.70	1.73–1.77	1.74–1.79
	8.34–8.50 (+0.18%)	1.9 (+11.8%)	4.70–4.75 (−1.36%)	1.3 (+18.2%)	4.67–4.72 (−1.26%)	1.0 (−9.1%)	0.02–1.61 (−5.29%)	1.77–1.80 (+2.00%)	1.77–1.81 (+1.42%)
G9708D1	8.12–8.31	2.3	4.62–4.76	3.0	4.62–4.68	1.5	0.00–3.09	1.74–1.76	1.74–1.80
	8.13–8.31 (+0.06%)		4.51–4.65 (−2.44%)		4.50–4.57 (−2.44%)			1.78–1.81 (+2.25%)	1.79–1.85 (+2.25%)
K5622A1	8.19–8.33	1.6	4.64–4.69	1.1	4.62–4.67	1.0	0.09–1.46	1.76–1.78	1.77–1.80
	8.17–8.30 (−0.30%)	1.6 (+0.0%)	4.55–4.60 (−1.93%)	1.1 (+0.0%)	4.53–4.58 (−1.94%)	0.9 (−10.0%)	0.07–1.46 (+0.0%)	1.79–1.81 (+1.69%)	1.80–1.83 (+1.68%)
K5628E1	8.23–8.36	1.5	4.67–4.74	1.6	4.66–4.72	1.3	0.02–1.66	1.74–1.77	1.75–1.79
	8.25–8.38 (+0.24%)	1.5 (+0.0%)	4.60–4.67 (−1.49%)	1.6 (+0.0%)	4.59–4.64 (−1.60%)	1.2 (−7.69%)	0.02–1.72 (+3.61%)	1.77–1.81 (+1.99%)	1.78–1.83 (+1.97%)
K5629B	8.04–8.27	2.8	4.57–4.74	3.6	4.55–4.66	2.2	0.02–3.92	1.73–1.76	1.74–1.81
	8.09–8.32 (+0.61%)	2.8 (+0.0%)	4.50–4.67 (−1.50%)	3.6 (+0.0%)	4.49–4.59 (−1.41%)	2.2 (+0.0%)	0.02–3.95 (+0.77%)	1.77–1.80 (+2.29%)	1.77–1.85 (+1.97%)
M8709E1	8.39–8.50	1.3	4.81–4.86	0.9	4.76–4.83	1.4	0.00–1.42	1.73–1.76	1.74–1.78
	8.39–8.50 (−0.06%)		4.76–4.80 (−1.16%)		4.70–4.77 (−1.16%)			1.75–1.78 (+1.11%)	1.76–1.80 (+1.11%)
Italy	8.10–8.86	9.0	4.88–5.05	3.5	4.61–4.89	5.9	0.12–7.33	1.66–1.80	1.74–1.82
	7.99–8.75 (−1.32%)		4.70–4.87 (−3.63%)		4.44–4.71 (−3.63%)			1.70–1.84 (+2.40%)	1.78–1.86 (+2.40%)
Bernard	8.02–8.58	6.8	4.79–4.95	3.1	4.68–4.82	3.0	0.06–4.73	1.67–1.76	1.71–1.79
	7.91–8.46 (−1.36%)		4.63–4.77 (−3.44%)		4.52–4.66 (−3.44%)			1.70–1.80 (+2.16%)	1.75–1.83 (+2.16%)
Finero	7.66–8.91	15.1	4.67–5.05	7.8	4.39–4.74	7.9	0.42–12.32	1.61–1.85	1.72–1.91
	7.59–8.83 (−0.92%)		4.49–4.85 (−3.82%)		4.22–4.56 (−3.82%)			1.66–1.91 (+2.81%)	1.77–1.97 (+2.81%)

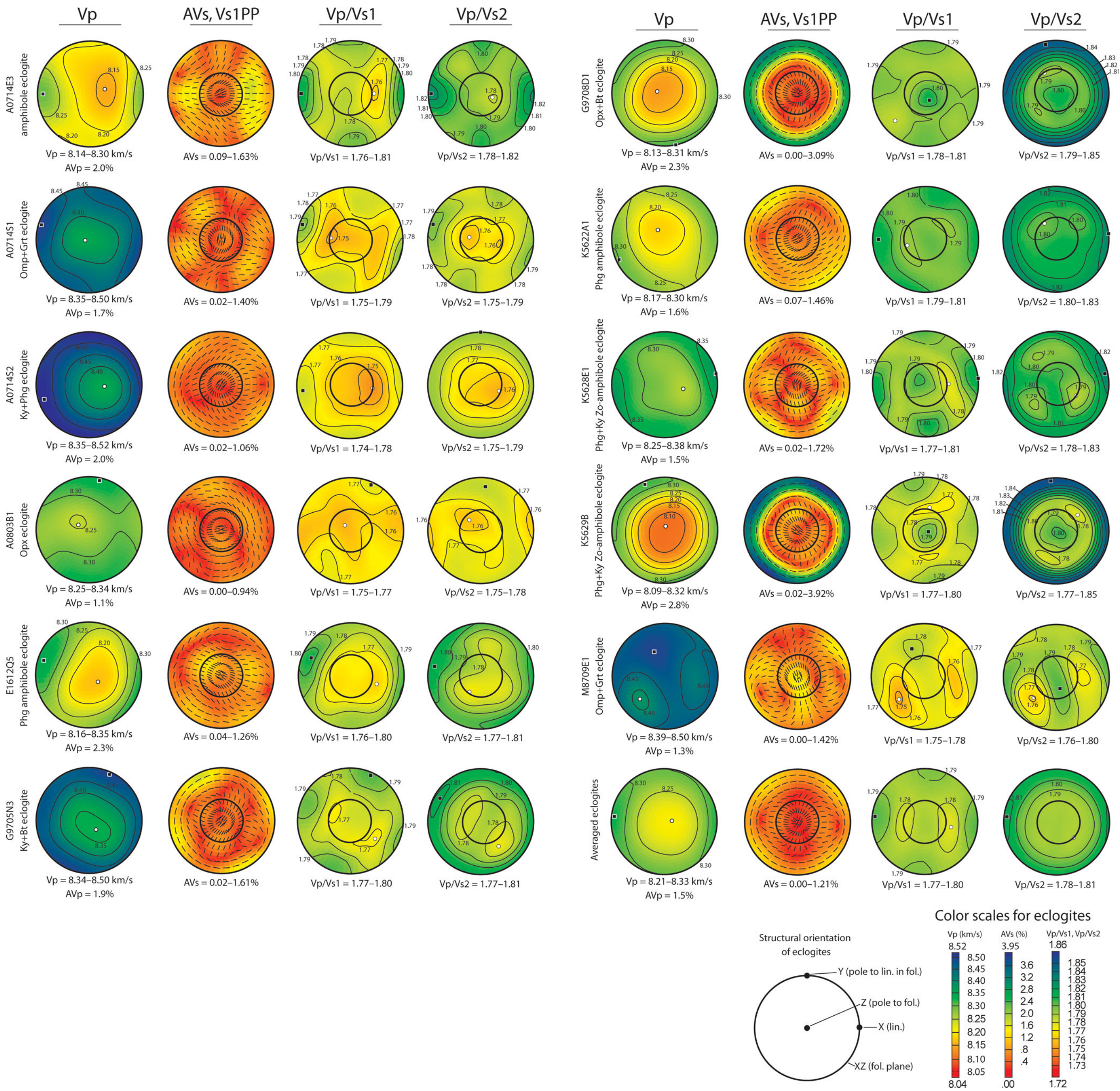

Figure 4. Lower-hemisphere, equal-area stereographic projections of seismic parameters for all eclogite samples (including a 'grand average'), looking down on the foliation plane as shown. Stereonets are grouped by sample in columns as follows: left, P-wave velocity (V_P, km s^{-1}); second from left, shear-wave anisotropy (AV_S, per cent) and fast shear-wave polarization plane (V_{S1}PP); third from left, V_P/V_{S1} ratio; fourth from left, V_P/V_{S2} ratio. Cool colours represent high values and warm colours represent low values for each seismic parameter. Shading is linear, and all samples are plotted using the same colour scale for each seismic parameter. V_P/V_{S1} and V_P/V_{S2} are plotted on the same scale. Black circle in centre of AV_S and V_P/V_{S1} diagrams represents the shear-wave window (35^o from vertical). Pressure–temperature conditions are 3.0 GPa and 750°C.

samples because pressure-induced increases in wave speed are counteracted by temperature-induced decreases in wave speed. The P-wave velocities of the eclogites are virtually unchanged from STP to peak conditions, whereas a ~1 per cent reduction is calculated for the peridotites. The S-wave velocities respond more to changes in conditions for both rock types: eclogite S-wave velocities are reduced ~1–2 per cent and peridotite S-wave velocities are reduced ~3.5–4 per cent. The changes increase eclogite V_P/V_S by 1–2 per cent and increase peridotite V_P/V_S by 2–3 per cent.

4.5 Calculated eclogite velocities

The calculated seismic properties of the eclogites at 'peak conditions' (3.0 GPa/750 °C) are compiled in Table 3 and Fig. 4. The stereonets are oriented such that the foliation is parallel to the perimeter of the stereonet and the lineation is E–W. The P-wave velocities and anisotropies range from 8.0–8.5 km s^{-1} and 1.0–2.8 per cent. The S-wave velocities and anisotropies range from 4.5–4.8 km s^{-1} and 0–3.9 per cent; V_P/V_{S1} varies from 1.74–1.81 and V_P/V_{S2} varies from 1.75–1.85. The elastic properties of omphacite and garnet are the most important for eclogite, and the near-isotropy of garnet and its weak CPOs means that omphacite is the primary source of anisotropy. Omphacite's fast axis for *P* waves is [001], and the orthorhombic or uniaxial symmetry of the CPOs and coaxial relationship with respect to the foliation and lineation in most samples, leads to the fast propagation direction for *P* waves being parallel to the lineation. The V_P/V_{S1} and V_P/V_{S2} maxima in the eclogites thus generally also parallel the lineation. A final contribution from the omphacite [001] CPOs is to orient the fast *S*-wave polarization plane perpendicular to the lineation (within the shear-wave window). This effect is observed in bimineralic samples (A0714S1 and M8709E1).

Phengite or biotite contribute to the foliation in micaceous eclogite, and their strong anisotropy contributes significantly to orienting the fast and slow *P* velocities parallel and perpendicular to the foliation, respectively. The slowest *P*-wave velocities in the mica-rich samples (G9708D1 and K5629B) are for waves propagating perpendicular to the foliation; velocities within the foliation are isotropic, yielding an approximately hexagonal symmetry. Micas also control the shear-wave anisotropy in eclogite (G9708D1 and K5629B), producing $AV_S = 3$–4 per cent parallel to the foliation and high V_P/V_{S1} perpendicular to the foliation.

Hornblende is slower and more anisotropic than omphacite, but its fast [001] axis contributes to the fast *P*-wave velocities parallel to the lineation. Because of its relatively low abundance—even in the amphibole eclogite and zoisite–amphibole eclogites—the effect of hornblende on rock anisotropy is secondary; the velocities of the two eclogites with the most hornblende are not different from the velocities of the others. Hornblende tends to rotate the fast V_S polarization planes towards the lineation (within the shear-wave window). Orthopyroxene is faster and less anisotropic than hornblende, but because of weak CPOs and low abundance, it generally has little effect on eclogite velocity, except in the sample with the most orthopyroxene (A0803B1, 16 per cent), where an orthopyroxene CPO that resembles omphacite in other samples yields a fast *P*-wave direction perpendicular to the lineation. Kyanite is fast and moderately anisotropic, but contributes minimally due to low abundance. A test calculation using Winkler *et al.*'s (2001) kyanite stiffness matrix for kyanite in A0714S2, which contains this mineral's maximum modal abundance in our study, revealed negligible seismic velocity differences (<1 per cent) from the calculation we report, which employs Vaughan & Guggenheim's (1978) sillimanite stiffness matrix. Zoisite is fast and moderately anisotropic, and the observed alignment of its fast [100] directions perpendicular to the foliation contributes to fast *P*-wave velocities in this direction, although the contribution is reduced by the low abundance of zoisite. Rutile, common but not abundant, is fast and moderately anisotropic, and serves mainly to maintain high velocities in eclogite, although the rutile CPO in A0803B1 contributes to fast velocities 45° to the foliation. Coesite is faster and more anisotropic than quartz, and its presence in eclogite at 'peak conditions' contributes primarily to faster velocities (e.g. A0714S1).

In summary, eclogite velocities are primarily controlled by garnet and omphacite modal abundances, and omphacite and mica CPOs. Eclogite is essentially isotropic except for micaceous rocks, which have fast and slow *P*-wave velocities parallel and perpendicular to the foliation.

4.6 Calculated peridotite velocities

The calculated seismic properties of three peridotites at peak conditions are compiled in Table 3 and Fig. 5. The *P*-wave velocities and anisotropies range from 7.6–8.8 km s^{-1} and 7–15 per cent. The *S*-wave velocities and anisotropies range from 4.2–4.9 km s^{-1} and 0–12 per cent, V_P/V_{S1} is 1.66–1.91 and V_P/V_{S2} is 1.75–1.97. Peridotite velocities are dominated by olivine, whose fast [100] direction for *P* waves is parallel to the lineation in A-type CPOs ('Italy') and subparallel to the lineation in E-type CPOs ('Bernard' and 'Finero') (e.g. Karato *et al.* 2008). As a result, *P*-wave velocities are fast parallel to the lineation and slow perpendicular to the lineation in all three peridotites. The V_P/V_{S1} and V_P/V_{S2} maxima mimic the V_P maxima, and the minima are perpendicular to the lineation in a wide girdle that spans most of the stereonet. This results in the lowest range of V_P/V_{S1} and V_P/V_{S2} (to a lesser extent) in the shear-wave window, most notably in 'Finero', where the biotite produces anomalously low V_P/V_{S1} (1.68) perpendicular to the foliation. The V_{S1} polarization planes strongly parallel the lineation because of the reinforcing effects of olivine and orthopyroxene anisotropy and CPOs. Shear-wave anisotropy reaches a minimum subparallel to the lineation for all samples because the middle range of V_{S1} and high range of V_{S2} occur along the lineation. The middle range of shear-wave anisotropy occurs within the shear-wave window for 'Italy' and 'Finero', whereas the middle to upper range occurs within the shear-wave window for 'Bernard'.

4.7 Comparison of eclogite velocities to previous studies

The eclogite velocities obtained in this study are similar to those measured in bimineralic eclogite with the pulse-transmission technique. Kern *et al.* (1999) measured mean $V_P = 7.90$–8.05 km s^{-1}, $AV_P \sim 2$ per cent, $Vs = 4.65$–4.74 km s^{-1} and $\delta V_S = 0.05$ km s^{-1} at 600 MPa in two bimineralic eclogites from the Dabie UHP belt in China. Their measured V_P are slower (likely due to incomplete closure of microcracks and as much as 13 per cent quartz in their samples), but their V_S are comparable. Ábalos *et al.* (2011) measured $V_P = 8.27$–8.39 km s^{-1}, $AV_P = 1$–3 per cent, $V_S = 4.70$–4.83 km s^{-1} and $AV_S = 0$–1 per cent at 600 MPa in fresh, massive eclogites from the Cabo Ortegal complex in Spain. Their results are comparable to ours. Fountain *et al.* (1994) measured $V_P = 8.24$–8.44 km s^{-1} and $AV_P = 1$–6.5 per cent at 600 MPa in eclogites from the Bergen Arc in Norway. Christensen (1996) measured $V_P = 8.05$–8.35 km s^{-1}, $V_S = 4.45$–4.74 km s^{-1}, and $V_P/V_S = 1.74$–1.82 at 1000 MPa for a mafic eclogite, which resembles our results.

Similar EBSD-based calculations of eclogite velocities have yielded more variable results. Ji *et al.* (2003) calculated $V_P = 8.67$–8.84 km s^{-1}, $AV_P = 1.4$–1.5 per cent, $V_S = 4.96$–5.03 km s^{-1} and $AV_S = 0$–1.41 per cent for coarse- and fine-grained eclogites from the Sulu region, China. Their calculated velocities are faster than ours because they only used stiffness matrices for garnet, omphacite and rutile and ignored minor, slower phases like quartz, which comprises up to 1.8 per cent of their rocks. Mauler *et al.* (2000) calculated $V_P = 7.96$–8.55 km s^{-1}, $AV_P = 1.1$–1.3 per cent, $V_S = 4.57$–4.90 km s^{-1} and $dV_S = 0.02$–0.05 km s^{-1}. Their results are comparable to ours. Bascou *et al.* (2001) calculated $V_P = 8.39$–8.75 km s^{-1}, $AV_P = 1.2$–2.9 per cent, $V_S = 4.84$–5.00 km s^{-1} and maximum $AV_S = 0.74$–2.02 per cent for eclogites from various UHP regions. Their calculated velocities are faster than ours and likely an overestimate because, like Ji *et al.* (2003), they ignored the contribution of minor, slower phases in their calculations. None of these authors scaled their calculations from STP or used coesite stiffnesses in their calculations. On the other hand, Kopylova *et al.* (2004) modelled $V_P \sim 8.1$ km s^{-1} and $V_S \sim 4.5$ km s^{-1} for chlorite-free eclogite under the Slave craton in Canada at 3.0 GPa using empirically and

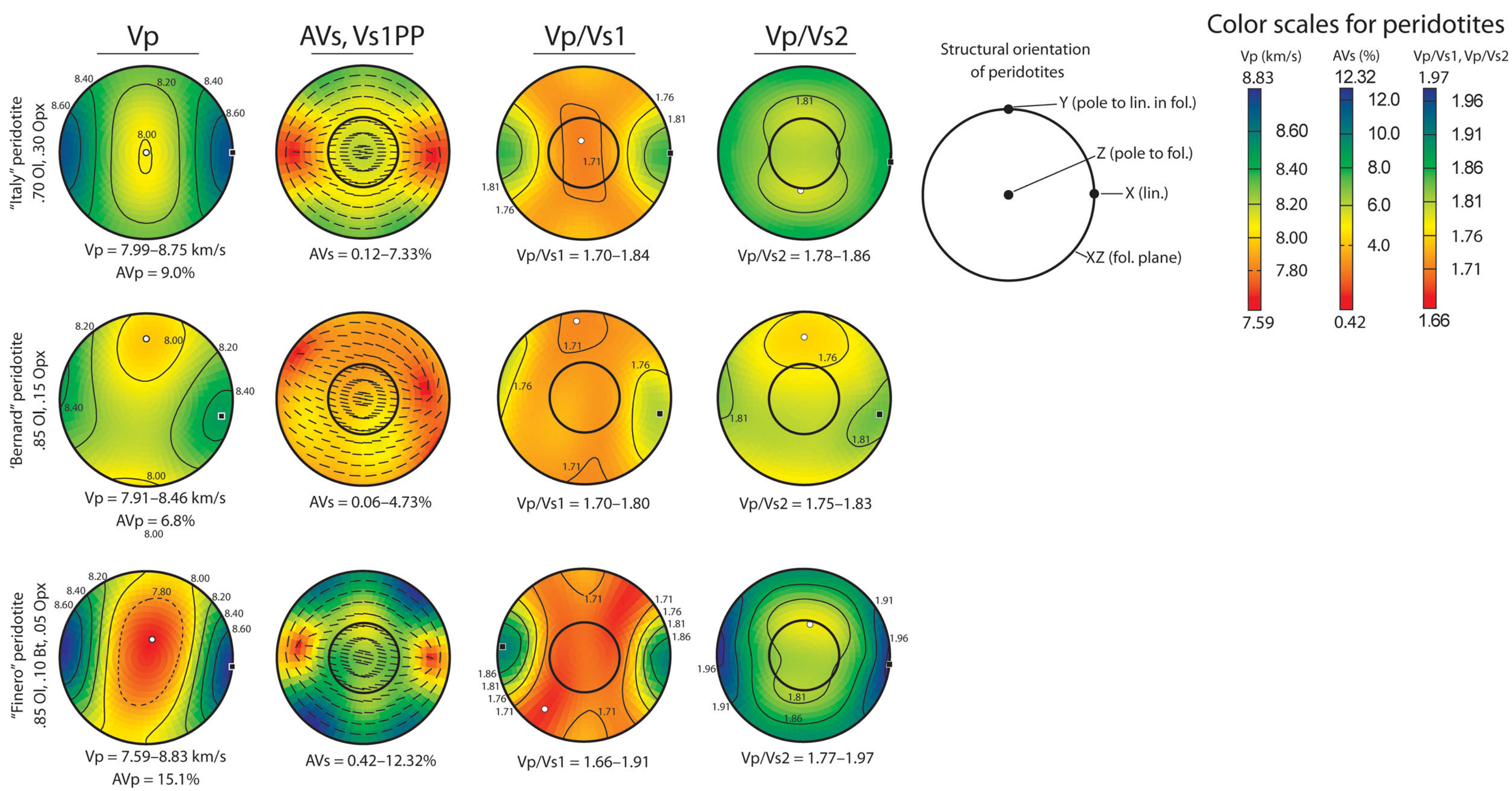

Figure 5. Lower-hemisphere, equal-area stereographic projections of seismic parameters for all peridotites, looking down on the foliation plane as shown. Stereonets are grouped by sample in columns as follows: left, *P*-wave velocity (V_P, km s^{-1}); second form left, shear-wave anisotropy (AV_S, per cent) and fast shear-wave polarization plane (V_{S1}PP); third from right, V_P/V_{S1} ratio; fourth from right, V_P/V_{S2} ratio. Cool colours represent high values and warm colours represent low values for each seismic parameter. Shading is linear, and all samples are plotted using the same colour scale for each seismic parameter. V_P/V_{S1} and V_P/V_{S2} are plotted on the same scale. Black circle in centre of AV_S and V_P/V_{S1} diagrams represents the shear-wave window (35° from vertical). Pressure–temperature conditions are 3.0 GPa and 750°C.

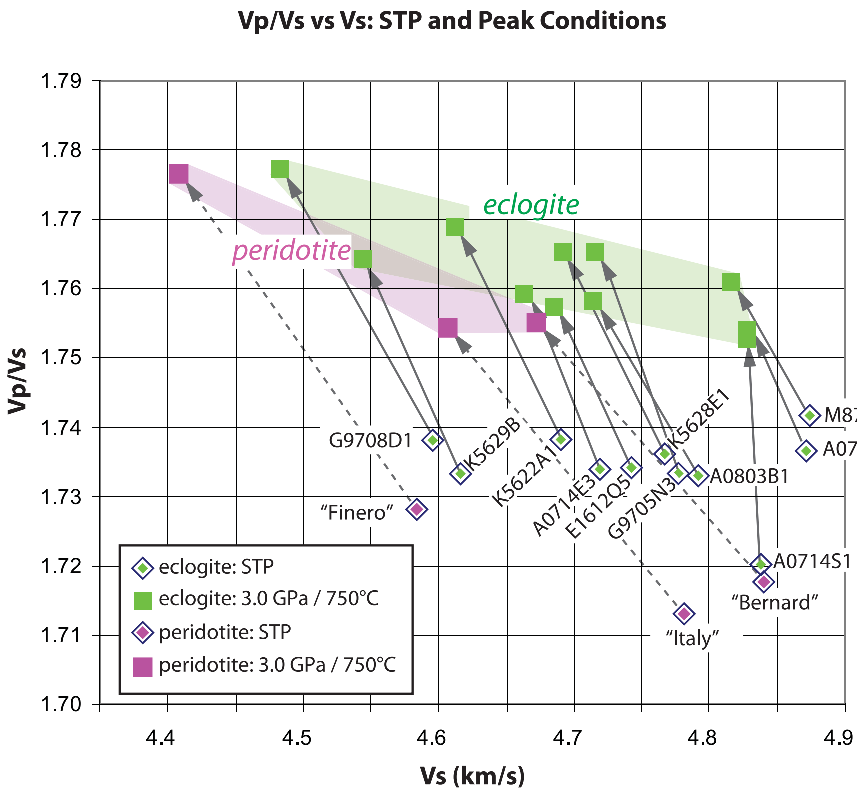

Figure 6. Calculated isotropic velocities for eclogites and peridotites from this study at STP (0.01 GPa, 25°C) and at 'peak conditions' (3.0 GPa, 750°C), using the excel macro of Hacker & Abers (2004). Each sample was matched to the calculated modal abundances and composition of solid-solution minerals indicated for the single-crystal stiffness matrices used in the 3-D, Mainprice-based calculations. For the eclogites with quartz, STP values were calculated using quartz and peak values were calculated with coesite. Peridotite is more responsive to the change in conditions than eclogite, which produces a tighter clustering of eclogites and peridotites at 'peak conditions' in V_p/V_s versus V_s space.

theoretically derived pressure and temperature derivatives of bulk-rock V_P, V_S, elastic moduli and density. Their eclogite velocities increase rapidly with pressure, reaching $V_P = 8.5$ and $9.0\,\mathrm{km\,s^{-1}}$ at 4.0 GPa and 6.0 GPa.

5 DISCUSSION

5.1 Distinguishing eclogite from peridotite using seismic parameters

Our results and all previous studies show that eclogite is a near-isotropic rock (4 per cent maximum anisotropy) over a broad range of compositions, mineralogies and structural fabrics. Minor and accessory phases have little effect on anisotropy, with the exception of mica. It is evident from Fig. 4 that the lowest values of shear-wave anisotropy for subhorizontally foliated micaceous eclogite are represented in the shear-wave window, meaning that subvertically incident shear waves undergo no splitting. Moderate values in the range of peridotite shear-wave anisotropy are represented in the shear-wave window, however, which may be a means of distinguishing between eclogite and peridotite. V_{S1} polarization planes strongly parallel the lineation in peridotite but are more variably oriented in eclogite.

5.2 V_P/V_S

Together, the V_P/V_S ratio and V_S can be an effective means of segregating rocks with similar P and S velocities into distinct domains. Fig. 6 displays the isotropic V_P/V_S ratio plotted versus V_{S1} for the eclogites and peridotites from this study, calculated at STP (0.01 GPa, 25°C) and 'peak conditions' (3.0 GPa, 750°C). Peridotite and eclogite are indistinguishable from one another at high pressure and temperature on the basis of V_P/V_S ratio, but V_S for eclogite can be considerably greater than that for peridotite, especially mica-bearing peridotite.

The high V_P/V_{S1} ratios that we calculate for eclogite at 'peak conditions' (up to 1.81) have been observed in other studies. Kern *et al.* (1999) extrapolated an average isotropic eclogite V_P/V_S of 1.78 at 1400 MPa and 570°C and Manghnani *et al.* (1974) measured V_P/V_S as high as 1.87 in unretrogressed eclogite. On the other hand, Gao *et al.* (2001) measured quite low V_P/V_S ratios in unaltered eclogite: 1.70–1.76.

Fig. 7 expands Fig. 6 into the anisotropic realm for rays sampling subhorizontally foliated rocks within the shear-wave window. Anisotropy and variability of propagation direction means that a plot of V_P/V_{S1} versus V_{S1} for a given sample occupies a field on the diagram (rather than a point) that contains the combinations of V_P/V_{S1} and V_{S1} for all rays in the shear-wave window. This field is non-uniform in that most rays sampling the shear-wave window have V_P/V_{S1} and V_{S1} values near the centre. Thus, we have colour-contoured each sample by 'ray density', which simply displays the percentage of rays sampling the shear-wave window (by colour) that have given combinations of V_P/V_{S1} and V_{S1} (the area of each subfield). The result for each sample is a set of concentric ovals with decreasing ray density from the centre. The rocks are plotted at STP (Fig. 7a) and 'peak conditions' (Fig. 7b). Velocities from the AK135 (Kennet *et al.* 1995) and PREM (Dziewonski & Anderson

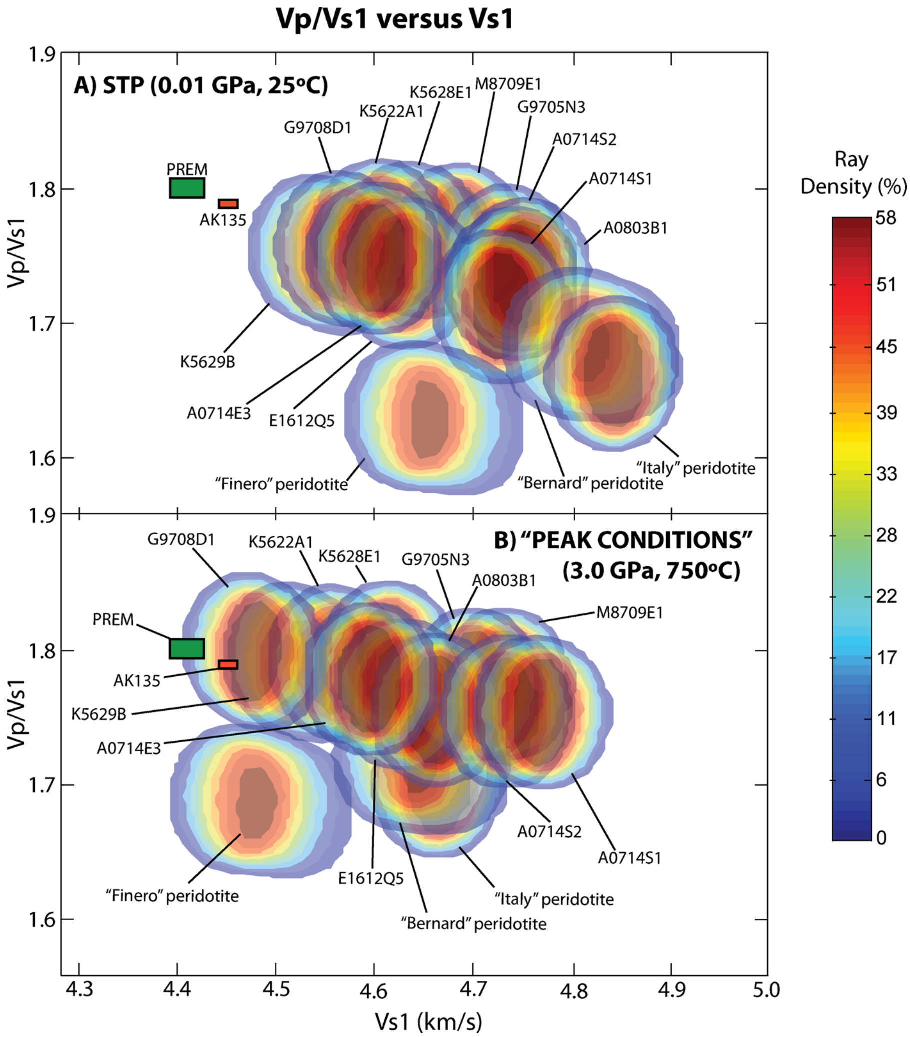

Figure 7. V_P/V_{S1} versus V_{S1} for subhorizontally foliated eclogites and peridotites from this study (multicoloured ovals) within the shear-wave window (35° from vertical). The 'ray density' colour scale represents the percentage of rays sampling the shear-wave window that have the given V_P/V_{S1} and V_{S1} values, and is displayed as contoured, multicoloured ovals. Warm colours indicate an abundance of discrete directions within the shear-wave window that have the specified combination of V_P/V_{S1} and V_{S1} values, whereas cool colours indicate that few directions have these values. Pressure–temperature conditions are (a) standard temperature and pressure (STP, 0.01 GPa and 25°C) and (b) 'peak conditions' (3.0 GPa and 750°C). The eclogites with quartz at STP have been calculated using coesite at 'peak conditions'. AK135 (78–120 km) and PREM (80–171 km) model velocities included as green and red boxes, respectively.

1981) models at 77–120 and 80–171 km depth are included for comparison, but we note that those models reflect the bulk Earth, not the subduction zone P–T conditions of 3 GPa and 750°C. The eclogites form a 'belt' of similar V_P/V_{S1} within a range of V_{S1}. At STP, the 'Italy' and 'Bernard' peridotites have lower V_P/V_{S1} and higher V_{S1} than eclogite and exhibit the same relationship to eclogite as Christensen's (1996) dunite and mafic eclogite in V_P/V_S versus V_S space (measured at 1000 MPa). The 'Finero' peridotite clearly occupies its own domain in V_P/V_{S1} versus V_{S1} space because its high anisotropy and the presence of biotite produce very low V_P/V_{S1} within the shear-wave window. At 'peak conditions' the peridotites still have lower V_P/V_{S1} than eclogite.

Low V_P/V_S has been observed in tomography studies of mantle wedges. Wagner *et al.* (2008) attributed low isotropic V_P/V_S (as low as 1.68) observed in the mantle wedge above the Chile–Peru flat slab to high orthopyroxene concentrations in peridotite (up to 40 per cent, producing V_P/V_S as low as 1.72) calculated using the elastic constants of Schutt & Lesher (2006). Soustelle & Tommasi (2010) and Hacker & Abers (2012) noted that such low V_P/V_S ratios could also be explained by elastic anisotropy inherent in deformed peridotite. Alternatively, we note that the biotite-bearing 'Finero' peridotite has similarly low V_P/V_S ratios in the shear-wave window because olivine and mica CPOs generate disparately high V_P/V_{S1} parallel to the lineation and low V_P/V_{S1} perpendicular to the foliation. Anomalously low V_P/V_{S1} measured from a mantle wedge may therefore represent metasomatized peridotite with subhorizontally oriented biotite. Such a fabric would be consistent with an upper mantle wedge dominated by corner flow. This is in contrast to conventional canon, which holds that micaceous phases such as serpentine in the mantle increase V_P/V_S (e.g. Hacker *et al.* 2003), and illustrates the importance of considering anisotropy and structural orientation in the interpretation of seismic data.

We have also provided the V_P/V_{S2} ratio for all of the eclogites and peridotites (Table 3). This is another form of data to use in assessing rock seismic properties, and is a feasible measurement in any shear-wave splitting study. Characterizing a lithology by both V_P/V_{S1} and V_P/V_{S2} may help reduce ambiguity in tomography and anisotropy studies. For instance, Boyd *et al.* (2004), in their study

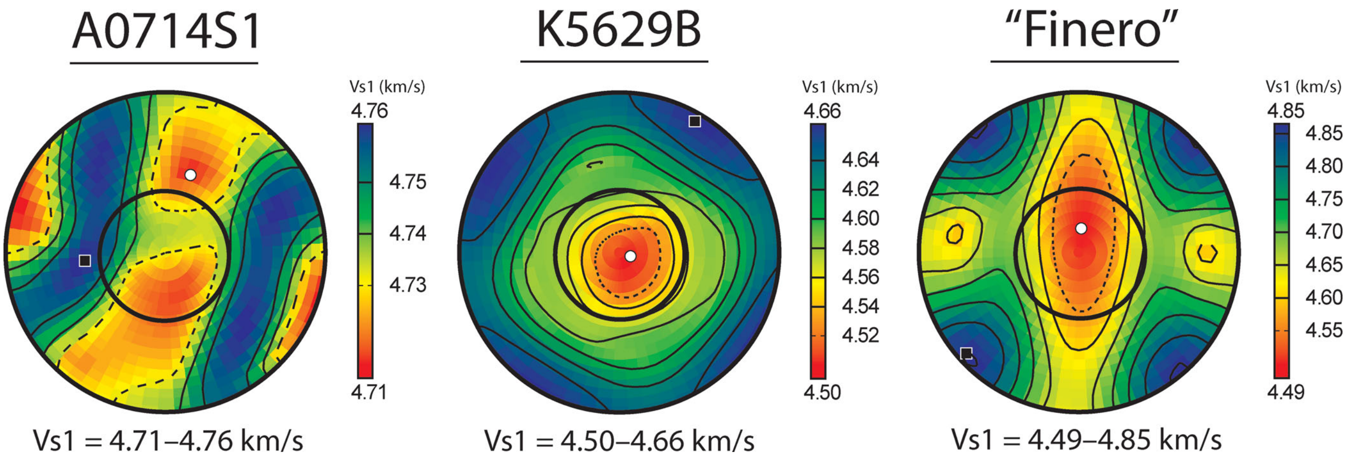

Figure 8. Fast shear-wave velocity structures in mica-free eclogite (A0714S1) and a micaceous peridotite ('Finero') are more complex than and not coaxial with their compressive-wave counterparts. Note (by comparison to Figs 4 and 5) that the fast shear-wave velocity structure is coaxial with the compressional-wave velocity structure for micaceous eclogite (K5629B), which contains abundant mica but is otherwise isotropic. Lower-hemisphere, equal-area stereographic projections are oriented the same as in Figs 4 and 5.

of foundering lithosphere under the Sierra Nevada of California, measured arrival times of *P* waves and both *S* waves and path-integrated attenuation of both *S* waves to invert for variations in velocities of *P* waves and both *S* waves and attenuation factors of both *S* waves. Their combined data revealed variations in V_P/V_S and transverse *S*-wave anisotropy and their tomographic inversions substantially reduced variance of the data, which suggests that it is expedient to incorporate the slow shear-wave in this fashion.

5.3 Symmetry of anisotropy

Our peridotite velocity diagrams (Fig. 5) indicate that orthorhombic velocity anisotropy for compressional waves in peridotite is a valid approximation; compressional wave velocities are fast in the *X* direction and similarly slow but distinct in the *Y* and *Z* directions. Given that there are five parameters in a hexagonally anisotropic system (also known as radial anisotropy and transverse isotropy) as opposed to nine in an orthorhombically anisotropic system, increased computational feasibility and the availability of code capable of modelling and inverting for the former but not the latter makes it desirable to characterize peridotite as hexagonally anisotropic. This approximation is less valid for peridotite than orthorhombic symmetry because compressional velocities in the *Y* and *Z* structural directions are not identical, although they are quite similar. Modelling peridotite as hexagonally anisotropic with a fast unique axis in the *X* direction is thus less robust than orthorhombic anisotropy, but still a reasonable approximation given the greater computational feasibility for the former.

The general isotropy we have calculated for eclogite means that modelling it using the two Lamé parameters necessary for an isotropic system is generally valid. We have seen (Table 3, Fig. 4) that eclogite anisotropy is sensitive to the presence of moderate quantities of mica, however (e.g. G9708D1, K5629B). Micas are the best approximation to hexagonal anisotropy of any mineral (Fig. 3) and it is clear from Fig. 4 that the phengite- and biotite-rich eclogites (K5629B and G9807D1) are hexagonally anisotropic for compressional waves with a unique, slow axis perpendicular to a fast foliation plane. Furthermore, A0714S1 (no mica), A0714S2 (minimal mica), and K5622A1 (minimal mica) are moderately hexagonally anisotropic for compressional waves, as well as the 'averaged' eclogites in Fig. 4, indicating that eclogite is adequately characterized by minimal or moderate hexagonal anisotropy, depending on the abundance of mica in the body being sampled by seismic waves.

It is informative to note that, in general, the *P*-wave anisotropy is not identical to the *S*-wave anisotropy. Most codes that model and invert for layers of anisotropy in Earth, such as *raysum* (Fredericksen & Bostock 2000), *do* make this assumption. Fig. 8 displays V_{S1} for two eclogites and a peridotite, and illustrates that only for eclogites with abundant mica are the compressional- and shear-wave velocity structures coaxial (both have hexagonal anisotropy). For all other rocks—eclogite and peridotite—the calculated fast and slow shear-wave velocity structures are more complex than their compressional-wave counterparts. It is clear, therefore, that coaxial 3-D compressional- and shear-wave velocity structures require (1) abundant highly anisotropic phase(s) with coaxial 3-D compressional- and shear-wave velocity structures and (2) an otherwise isotropic rock. This is achieved in micaceous eclogite but not in any peridotite we have calculated; this detail should be acknowledged in studies assuming a unique axis of anisotropy for compressional and shear-waves sampling the lower crust and upper mantle.

5.4 Connection of eclogite and peridotite anisotropy to petrotectonic regimes

The orthorhombic anisotropy (or fast-axis hexagonal anisotropy as a second-best approximation) of peridotite is central to being able to use seismic waves to infer flow direction within the mantle. Note that the uniaxial velocity anisotropy or near-isotropy of eclogite renders this impossible; instead, one could in principle use the velocity anisotropy of eclogite to infer the orientation of flow planes. Such flow planes may reveal the kinematics of underplating eclogite in orogenic roots (e.g. Saleeby *et al.* 2003) or Rayleigh–Taylor instabilities with a sheet-like, 2-D geometry (Brownlee *et al.* 2011). Sufficiently micaceous eclogite in these settings (likely from metasomatism) could produce a vertical slow unique axis of anisotropy from horizontal flattening or a horizontal slow unique axis of anisotropy from vertical flattening. Uniaxial eclogite anisotropy could also be used to resolve the orientation of deviatoric stress at the time of crystallization, potentially yielding further kinematic and tectonic inferences.

Zones of subducted continental crust like the purported active intracontinental subduction zone under the Pamir (e.g. Burtman & Molnar 1993) contain sufficient K_2O and Al_2O_3 to form phengite as a stable phase at eclogitic pressures and temperatures. In such cases, anisotropy perpendicular to the subducting slab due to the presence of phengite is expected. Careful attention in forward modeling—and inverting for such anisotropy—may reveal further details of low-velocity zones inferred to represent subducted continental crust (e.g. Roecker 1982) and enable further evaluation of the suggestions that such observations represent subducted continental lithosphere.

Our results for isotropic (Fig. 6) and anisotropic (Figs 4, 5 and 7) velocities indicate that the compositional effect of mixing mafic rock into the mantle should not change compressional- or shear-wave velocities, but may slightly increase V_P/V_S. We note, however, that because descending mafic rock is colder than the surrounding mantle, an accompanying reduction in temperature should increase compressional- and shear-wave velocities. Deconvolving these compositional and temperature effects is therefore crucial in identifying and characterizing mantle eclogite in its various tectonic contexts.

6 CONCLUSIONS

We have computed the 3-D variation of seismic parameters for a range of eclogite and peridotite compositions and structural fabrics, both at STP and at 'peak conditions' (3.0 GPa, 750°C). For eclogite, the *P*-wave velocities and anisotropies range from 8.0–8.5 km s^{-1} and 1.0–2.8 per cent. The *S*-wave velocities and anisotropies range from 4.5–4.8 km s^{-1} and 0–3.9 per cent. For peridotite, the *P*-wave velocities range from 7.6–8.8 km s^{-1} and 7–15 per cent. The *S*-wave velocities and anisotropies range from 4.2–4.9 km s^{-1} and 0–12 per cent. Eclogite is only weakly seismically anisotropic, and while increased mica content markedly increases anisotropy, typical mica abundances are too low in eclogite for its anisotropy to approach that of peridotite. V_P/V_{S1} is generally higher in eclogite than peridotite. Anomalously low V_P/V_{S1} is observed in vertically incident rays sampling subhorizontally foliated, metasomatized peridotite containing biotite.

Our results indicate that peridotite is best modelled using orthorhombic symmetry. Hexagonal symmetry with a fast unique axis is a less robust but reasonable characterization of peridotite and hexagonal symmetry with a slow unique axis is a robust approximation for micaceous eclogite. We stress that it is important to consider anisotropy in teleseismic studies and tomographic inversions. While it is challenging and computationally more demanding to incorporate the effect of anisotropy in such studies, attention to these details may be an effective method for eliminating lithologic and geodynamic ambiguities inherent in isotropic assumptions.

ACKNOWLEDGMENTS

This project was supported by NSF grants EAR-0838269, EAR-0745588, and EAR-0929777. Gareth Seward helped collect and process the EBSD data; Sarah Brownlee helped with the Mainprice software and MATLAB code; Monica Erdman helped with the Mainprice software; discussions with Ryan Porter about anisotropy symmetry systems helped us understand the applicability of our calculations to real seismic waveforms. We thank Sandra Piazolo and an anonymous reviewer for their helpful comments, which improved the quality of this manuscript.

REFERENCES

Ábalos, B., Fountain, D.M., Gil Ibarguchi, J.I. & Puelles, P., 2011. Eclogite as a seismic marker in subduction channels: seismic velocities, anisotropy, and petrofabric of Cabo Ortegal eclogite tectonies (Spain), *Geol. Soc. Am. Bull.,* **123,** 439–456.

Abramson, E.H., Brown, J.M., Slutsky, L.J. & Zaug, J., 1997. The elastic constants of San Carlos olivine to 17 GPa, *J. geophys. Res.,* **102,** 12 253–12 263.

Aleksandrov, K.S. & Ryzhova, T.V., 1961a. The elastic properties of rock-forming minerals: pyroxenes and amphiboles, *Bull. Acad. Sci. USSR, Geophys. Ser.,* **9,** 871–875.

Aleksandrov, K.S. & Ryzhova, T.V., 1961b. Elastic properties of rock-forming minerals. II. Layered silicates, *Bull. Acad. Sci. USSR, Geophys. Ser.,* **9,** 1165–1168.

Angel, R.J., Mosenfelder, J.L. & Shaw, C.S.J., 2001. Anomalous compression and equation of state of coesite, *Phys. Earth planet. Inter.,* **124,** 71–79.

Babuska, V., Fiala, J., Kumazawa, M., Ohno, I. & Sumino, Y., 1978. Elastic properties of garnet solid-solution series, *Phys. Earth planet. Inter.,* **16,** 157–176.

Bascou, J., Barroul, G., Vauchez, A., Mainprice, D. & Egydio-Silva, M., 2001. EBSD-measured lattice-preferred orientations and seismic properties of eclogites, *Tectonophysics,* **342,** 61–80.

Bass, J.D., 1995. Elasticity of minerals, glasses, and melts, in *Mineral Physics & Crystallography: A Handbook of Physical Constants,* pp. 46–63, ed. Ahrens, T.J., Am. geophys. Un., Washington, DC.

Bensen, G.D., Ritzwoller, M.H. & Shapiro, N.M., 2008. Broadband ambient noise surface wave tomography across the United States, *J. geophys. Res.,* **113,** B05306.

Bhagat, S.S. & Bass, J.D., 1992. Single-crystal elastic properties of omphacite-C2/c by Brillouin spectroscopy, *J. geophys. Res.,* **97,** 6483–6848.

Biryol, C.B., Zandt, G., Beck, S.L., Ozacar, A.A., Adiyaman, H.E. & Gans, C.R., 2010. shear wave splitting along a nascent plate boundary: the North Anatolian Fault Zone, *Geophys. J. Int.,* **181,** 1201–1213.

Boyd, O.S., Jones, C.H. & Sheehan, A.F., 2004. Foundering lithosphere imaged beneath the southern Sierra Nevada, California, USA, *Science,* **305,** 660–662.

Bostock, M.G., 1999. Seismic imaging of lithospheric discontinuities and continental evolution, *Lithos,* **48,** 1–16.

Brownlee, S.J., Hacker, B.R., Salisbury, M., Seward, G., Little, T.A., Baldwin, S.L. & Abers, G.A., 2011. Predicted velocity and density structure of the exhuming Papua New Guinea ultrahigh-pressure terrane, *J. geophys. Res.,* **116,** B08206.

Burtman, V.S. & Molnar, P., 1993. Geological and geophysical evidence for deep subduction of continental crust beneath the Pamir, *Special Paper 281*, Geological Society of America, Boulder, CO.

Cawthorn, R.G., 1975. "Amphibole peridotite-metagabbro complex, Finero, northern Italy, *J. Geol.,* **83,** 437–454.

Christensen, N.I., 1979. Compressional wave velocities in rocks at high temperatures and pressures, critical thermal gradients, and crustal low-velocity zones, *J. geophys. Res.,* **84,** 407–412.

Christensen, N.I., 1996. Poisson's ratio and crustal seismology, *J. geophys. Res.,* **101,** 3139–3156.

Coleman, R.G., Lee, D.E., Beatty, L.B. & Brannock, W.W., 1965. Eclogites and eclogites: their differences and similarities, *Geol. Soc. Am. Bull.,* **76,** 483–508.

Cuthbert, S.J., Carswell, D.A., Krogh-Ravna, E.J. & Wain, A., 2000. Eclogites and eclogites in the Western Gneiss Region, Norwegian Caledonides, *Lithos,* **52,** 165–195.

Aspiroz, M.D., Lloyd, G.E. & Fernández, C., 2007. Development of lattice preferred orientation in clinoamphiboles deformed under low-pressure metamorphic conditions. A SEM/EBSD study of metabasites from the Aracena metamorphic belt (SW Spain), *J. Struct. Geol.,* **29,** 629–645.

Dziewonski, A.M. & Anderson, D.L., 1981. Preliminary reference Earth model, *Phys. Earth planet. Inter.,* **25,** 297–356.

Ekström, G. & Dziewonski, A.M., 1998. The unique anisotropy of the Pacific upper mantle, *Nature,* **394,** 168–172.

Erdman, M.E., Hacker, B.R., Zandt, G. & Seward, G., in review. Seismic anisotropy of the crust: electron backscatter diffraction measurements from the basin and range.

Eskola, P., 1921. *On the Eclogites of Norway,* Klasse, No. 8, pp. 1–118, Viden. Skrifter. 1 Mat-Naturv.

Fountain, D.M., Boundy, T.M., Austrheim, H. & Rey, P., 1994. Eclogite-facies shear zones—deep crustal reflectors? *Tectonophysics,* **232,** 411–424.

Fredericksen, A.W. & Bostock, M.G., 2000. Modelling teleseismic waves in dipping anisotropic structures, *Geophys. J. Int.,* **141,** 401–412.

Gao, S., Kern, H., Jin, Z., Popp, T., Jin, S., Zhang, H. & Zhang, B., 2001. Poisson's ratio of eclogite: the role of retrogression, *Earth planet. Sci. Lett.,* **102,** 523–531.

Hacker, B.R., 2006. Pressures and temperatures of ultrahigh-pressure metamorphism: implications for UHP tectonics and H2O in subducting slabs, *Int. Geol. Rev.,* **48,** 1053–1066.

Hacker, B.R., 2008. H2O subduction beyond arcs, *Geochem. Geophys. Geosyst.,* **9,** Q03001, doi:10.1029/2007GC001707.

Hacker, B.R. & Christie, J.M., 1990. Brittle/ductile and plastic/cataclastic transitions in experimentally deformed and metamorphosed amphibolite, *Geophys. Monogr.,* **56,** 127–147.

Hacker, B.R., Abers, G.A. & Peacock, S.M., 2003. Subduction factory 1. Theoretical mineralogy, densities, seismic wave speeds, and H2O contents, *J. geophys. Res.,* **108**(B1), 2029, doi:10.1029/2001JB001127.

Hacker, B.R. & Abers, G.A., 2004. Subduction factory 3: an Excel worksheet and macro for calculating the densities, seismic wave speeds, and H2O contents of minerals and rocks at pressure and temperature, *Geochem. Geophys. Geosyst.,* **5,** Q01005, doi:10.1029/2003GC000614.

Hacker, B.R. & Abers, G.A., 2012. Subduction factory 5: unusually low Poisson's ratios in subduction zones from elastic anistoropy of peridotite, *J. geophys. Res.,* **117,** B06308, doi:10.1029/2012JB009187.

Helmstaedt, H., Anderson, O.L. & Gavasci, A.T., 1972. Petrofabric studies of eclogite, spinel-websterite, and spinel-lherzolite xenoliths from kimberlite-bearing breccia pipes in southeastern Utah and northeastern Arizona, *J. geophys. Res.,* **77,** 4350–4365.

Hetényi, G., Cattin, R., Brunet, F., Bollinger, L., Vergne, J., Nábělek, J. & Diament, M., 2007. Density distribution of the India plate beneath the Tibetan plateau: geophysical and petrological constraints on the kinetics of lower-crustal eclogitization, *Earth planet. Sci. Lett.,* **264,** 226–244.

Hess, H.H., 1964. Seismic Anisotropy of the uppermost mantle under oceans, *Nature,* **203,** 629–631.

Ji, S., Saruwatari, K., Mainprice, D., Wirth, R., Xu, Z. & Xia, B., 2003. Microstructures, petrofabrics and seismic properties of ultra high-pressure eclogites from Sulu region, China: implications for rheology of subducted continental crust and origin of mantle reflections, *Tectonophysics,* **370,** 49–76.

Kaneshima, S. & Silver, P.G., 1995. Anisotropic loci in the mantle beneath central Peru, *Phys. Earth planet. Inter.,* **88,** 257–272.

Karato, S., Jung, H., Katayama, I. & Skemer, P., 2008. Geodynamic significance of seismic anisotropy of the upper mantle: new insights from laboratory studies, *Annu. Rev. Earth Planet. Sci.,* **36,** 59–95.

Kern, H., Gao, S., Jin, Z., Popp, T. & Jin, S., 1999. Petrophysical studies on rocks from the Dabie ultrahigh-pressure (UHP) metamorphic belt, Central China: implications for the composition and delamination of the lower crust, *Tectonophysics,* **301,** 191–215.

Kennet, B.L.N., Engdahl, E.R. & Buland, R., 1995. Constraints on seismic velocities in Earth from traveltimes, *Geophys. J. Int.,* **122,** 108–124.

Kopylova, M.G., Lo, J. & Christensen, N.I., 2004. Petrological constraints on seismic properties of the Slave upper mantle (Northern Canada), *Lithos,* **77,** 493–510.

Kretz, R., 1983. Symbols for rock-forming minerals, *American Mineralogist,* **68,** 277–279.

Krogh, E.J., 1977. Evidence of Precambrian continent-continent collision in Western Norway, *Nature,* **267,** 17–19.

Lakshtanov, D.L., Sinogeikin, S.V. & Bass, J.D., 2007. High-temperature phase transitions and elasticity of silica polymorphs, *Phys. Chem. Miner.,* **34,** 11–22.

Mainprice, D., 1990. A Fortran program to calculate seismic anisotropy from the lattice preferred orientation of minerals, *Comput. Geosci.,* **16,** 385–393.

Mainprice, D., 2007. Seismic anisotropy of the deep Earth from a mineral and rock physics perspective, in *Treatise on Geophysics,* pp. 437–491, Vol. 2, ed. Price, G.D., Elsevier, Amsterdam.

Mainprice, D., Bascou, J., Cordier, P. & Tommasi, A., 2004. Crystal preferred orientations of garnet: comparison between numerical simulations and electron back-scattered diffraction (EBSD) measurements in naturally deformed eclogites, *J. Struct. Geol.,* **26,** 2089–2102.

Manghnani, M.H., Ramananantandro, R. & Clark, S.P., 1974. Compressional and shear wave velocities in granulite facies rocks and eclogites to 10 kbar, *J. geophys. Res.,* **79,** 5427–5446.

Mao, Z., Jiang, F. & Duffy, T.S., 2007. Single-crystal elasticity of zoisite Ca2Al3Si3O12(OH) by Brillouin scattering, *Am. Miner.,* **92,** 570–576.

Marone, F., Gung, Y. & Ramanowicz, B., 2008. Three-dimensional radial anisotropic structure of the North American upper mantle from inversion of surface waveform data, *Geophys. J. Int.,* **171,** 206–222.

Mauler, A., Burlini, L., Kunze, K., Philippot, P. & Burg, J.P., 2000. P-wave anisotropy in eclogites and relationship to the omphacite crystallographic fabric, *Phys. Chem. Earth,* **25,** 119–126.

Mehl, L., Hacker, B.R., Hirth, G. & Kelemen, P.B., 2003. Arc-parallel flow within the mantle wedge: Evidence from the accreted Talkeetna arc, south central Alaska, *J. geophys. Res.,* **108**(B8), 2375, doi:10.1029/2002JB002233.

Monsalve, G., Sheehan, A., Rowe, C. & Rajaure, S., 2008. Seismic structure of the crust and the upper mantle beneath the Himalayas: evidence for eclogitization of lower crustal rocks in the Indian Plate, *J. geophys. Res.,* **113,** B08315, doi:10.1029/2007JB005424.

Nakamura, D., 2003. Stability of phengite and biotite in eclogites and characteristics of biotite- or orthopyroxene-bearing eclogites, *Contrib. Miner. Petrol.,* **145,** 550–567.

Nesse, W.D., 1991. Introduction to Optical Mineralogy, Oxford University Press, Inc., New York, USA, 335 pp.

Nye, J.F., 1957. Physical Properties of Crystals, The Clarendon Press, Oxford, UK, 322 pp.

Pearce, M.A., Wheeler, J. & Prior, D.J., 2011. Relative strength of mafic and felsic rocks during amphibolite faies metamorphism and deformation, *J. Struct. Geol.,* **33,** 662–675.

Pera, E., Mainprice, D. & Burlini, L., 2003. Anisotropic seismic properties of the upper mantle beneath the Torre Alfina area (Northern Apennines, Central Italy), *Tectonophysics,* **370,** 11–30.

Poli, S. & Schmidt, M.W., 1998. The high-pressure stability of zoisite and phase relationships of zoisite-bearing assemblages, *Contrib. Miner. Petrol.,* **130,** 162–175.

Porter, R., Zandt, G. & McQuarrie, N., 2011. Pervasive lower-crustal seismic anisotropy in Southern California: evidence for underplated schists and active tectonics, *Lithosphere,* **3,** 201–220.

Roecker, S.W., 1982. Velocity structure of the Pamir-Hindu Kush region: possible evidence of subducted crust, *J. geophys. Res.,* **87,** 945–959.

Saleeby, J., Ducea, M. & Clemens-Knott, D., 2003. Production and loss of high-density batholithic root, southern Sierra Nevada, California, *Tectonics,* **22,** 1064.

Savage, M.K., 1999. Seismic anisotropy and mantle deformation: what have we learned from shear wave splitting? *Rev. Geophys.,* **37,** 65–106.

Schutt, D.L. & Lesher, C.E., 2006. Effects of melt depletion on the density and seismic velocity of garnet and spinel lherzolite, *J. geophys. Res.,* **111,** B05401.

Shapiro, N.M., Ritzwoller, M.H., Molnar, P. & Levin, V., 2004. Thinning and flow of Tibetan crust constrained by seismic anisotropy, *Science,* **305,** 233–236.

Silver, P.G., 1996. Seismic anisotropy beneath the continents: probing the depths of geology, *Annu. Rev. Earth Planet. Sci.,* **24,** 385–432.

Soustelle, V., Tommasi, A., Demouchy, S. & Ionov, D.A., 2010. Deformation and fluid-rock interaction in the supra-subduction mantle: microstructures and water contents in peridotite xenoliths from the Avacha volcano, Kamchatka, *J. Petrol.,* **51,** 363–394.

Soustelle, V. & Tommasi, A., 2010. Seismic properties of the supra-subduction mantle: Constraints from peridotite xenoliths from the Avacha volcano, southern Kamchatka, *Geophys. Res. Lett.,* **37,** L13307, doi:10.1029/2010GL043450.

Tatham, D.J., Lloyd, G.E., Butler, R.W.H. & Casey, M., 2008. Amphibole and lower crustal seismic properties, *Earth planet. Sci. Lett.,* **267,** 118–128.

Vaughan, M.T. & Weidner, D.J., 1978. The relationship of elasticity and crystal structure in andalusite and sillimanite, *Phys. Chem. Miner.,* **3,** 133–144.

Vaughan, M.T. & Guggenheim, S., 1986. Elasticity of muscovite and its relationship to crystal structure, *J. geophys. Res.,* **91,** 4657–4664.

Wagner, L.S., Anderson, M.L., Jackson, J.M., Beck, S.L. & Zandt, G., 2008. Seismic evidence for orthopyroxene enrichment in the continental lithosphere, *Geology,* **36,** 935–938.

Warren, L.M., Snoke, J.A. & James, D.E., 2008. S-wave velocity structure beneath the high lava plains, Oregon, from Rayleigh-wave dispersion inversion, *Earth planet. Sci. Lett.,* **274,** 121–131.

Webb, S.L. & Jackson, I., 1993. The pressure dependence of the elastic moduli of single-crystal orthopyroxene (MG0.8FE0.2)SIO3, *Euro. J. Miner.,* **5,** 1111–1119.

Weiss, T., Siegesmund, S., Rabbel, W., Bohlen, T. & Pohl, M., 1999. Seismic velocities and anisotropy of the lower continental crust: a review, *Pure appl. Geophysics,* **156,** 97–122.

Weidner, D.J. & Carleton, H.R., 1977. Elasticity of coesite, *J. geophys. Res.,* **82,** 1334–1346.

Wenk, H., Cottaar, S., Tome, C.N., McNamara, A. & Romanowicz, B., 2011. Deformation in the lowermost mantle: from polycrystal plasticity to seismic anisotropy, *Earth planet. Sci. Lett.,* **306,** 33–45.

Winkler, B., Hytha, M., Warren, M.C., Milman, V., Gale, J.D. & Schreuer, J., 2001. Calculation of the elastic constants of the Al2SiO5 polymorphs andalusite, sillimanite and kyanite, *Zeitschrift Für Kristallographie,* **216,** 67–70.

APPENDIX

Sample descriptions. UTM locations are in zone 32V.

A0714E3 Vågsøy. UTM: 0293058 6872796. Eclogite tectonite with elongate, subhedral–anhedral clinopyroxene, garnet, and phengite from 50–500 μm long; green amphibole is exclusively mm-scale porphyroclasts. Clinopyroxene has weak undulatory extinction; some have low-angle subgrains.

A0714S1 Måløy. UTM: 0300707 6878616. Eclogite tectonite with elongate, subhedral–anhedral clinopyroxene, garnet, and quartz up to 2 mm long.

A0714S2 Måløy. UTM: 0300707 6878616. Eclogite tectonite with elongate, subhedral–anhedral clinopyroxene and garnet up to 5 mm long; phengite and kyanite are 200–300 μm. Clinopyroxene and kyanite have strong undulatory extinction and well-developed subgrains.

A0803B1 Sula. UTM: 0348909 6924027. Unfoliated eclogite with equant anhedral garnet up to 3 mm in a matrix of equant, anhedral polygonized clinopyroxene and orthopyroxene from 100 μm to 3 mm. Biotite includes both tabular primary grains within clinopyroxene and minor retrograde rims on rutile.

E1612Q5 Hellesylt. UTM: 0386325 6884503. Eclogite tectonite with elongate, subhedral–anhedral clinopyroxene, garnet, and phengite up to 5 mm long; green amphibole forms equant 200 μm grains interstitial to clinopyroxene.

G9705N3 Gødøya. UTM: 0347685 6931616. Retrogressed eclogite tectonite with elongate, subhedral–anhedral 400–500 μm long clinopyroxene, garnet, and kyanite. Tabular biotite grains to 800 μm.

G9708D1 Otrøy. UTM: 0383694 6958620. Elongate–equant subhedral 2–6 mm garnets and anhedral tabular 2–6 mm clinopyroxene and orthopyroxene. Grain long axes are parallel to 500–1000 μm primary biotite. Equant green–brown pleochroic amphibole rims some biotite and is likely retrograde.

K5622A1 Vollstein. UTM: 0308467 6805341. Equigranular eclogite with euhedral 400 μm garnet in anhedral, similarly sized clinopyroxene, green amphibole and phengite.

K5628E1 Drøsdal. UTM: 0295087 6796869. Unusual eclogite: elongate clinopyroxene up to 1 cm and elongate muscovite up to 3 mm dotted with 50–200 equant garnet; zoisite and kyanite in clots of ~200 μm grains.

K5629B Hovden. UTM: 0295295 6802276. Coronitic eclogite. Equant, ~500–1000 μm diameter clinopyroxene and green amphibole between 500–100 μm thick garnet coronae surrounding fine-grained (<200 μm) mats of kyanite + phengite + zoisite. Green amphibole has moderate–strong undulatory extinction and abundant subgrains.

M8709E1 Skodje. UTM: 0373120 6934412. Eclogite tectonite of tabular, 100–500 clinopyroxene and garnet. Clinopyroxene has weak undulatory extinction and subgrains. Equant brown amphibole is likely retrograde.